High-precision proton-proton bremsstrahlung measurements at 190 MeV

M. Mahjour-Shafiei, J. C. S. Bacelar, M. D. Cozma, M. J. van Goethem,* M. N. Harakeh, M. Hoefman, H. Huisman, N. Kalantar-Nayestanaki,† H. Löhner, J. G. Messchendorp, R. W. Ostendorf, S. Schadmand,‡ O. Scholten, M. Volkerts, and H. W. Wilschut

Kernfysisch Versneller Instituut, Zernikelaan 25, 9747 AA Groningen, The Netherlands

(Received 27 November 2003; published 31 August 2004)

Two high-accuracy measurements of cross sections and analyzing powers for the proton-proton bremsstrahlung reaction have been performed at 190 MeV beam energy. These measurements provide not only the most accurate exclusive cross-section and analyzing-power data to date, but also a wide phase-space coverage. Thus, an accurate test of nucleon-nucleon interaction models is made feasible. The experimental setup and the analysis procedure are discussed in detail. Microscopic calculations and calculations based on the soft-photon theorem show deficiencies in explaining the bulk of the data.

DOI: 10.1103/PhysRevC.70.024004 PACS number(s): 25.10.+s, 13.75.Cs, 25.20.Lj

I. INTRODUCTION

One of the most fundamental problems in nuclear physics is that of understanding the strong force acting between nucleons. The simplest way to investigate this force is by studying the two-nucleon system either in the bound state (deuteron) or by means of elastic nucleon-nucleon (*NN*) scattering. The most modern *NN* potential models describe the world data set for *NN* scattering with a reduced χ^2 close to unity [1–3]. Since the predictions of different potential models for elastic *NN* scattering are nearly the same, they are said to be "data-equivalent." It is desirable to test the predictions of any of these modern potential models with reactions other than elastic scattering with different kinematic constraints. The simplest *NN*-scattering process going beyond elastic scattering is the $N+N \rightarrow N+N+\gamma$ or the bremsstrahlung reaction referred to hereafter as $NN\gamma$. By measuring physical observables for this process and comparing the results with the predictions of potential models one hopes for a better understanding of this process and thereby to gain more insight into the *NN* interaction dynamics than what is provided by the elastic channel.

In 1949, Ashkin and Marshak studied aspects of the proton-proton interaction not probed by elastic scattering in reactions resulting in bremsstrahlung for the first time [4]. Low proved in 1958 that in a series expansion in the photon momentum the first two terms of the scattering amplitude can be expressed exactly in terms of the elastic amplitude [5]. Any realistic model should converge to this expansion in the limit of the photon momentum going to zero. Inspired by the soft-photon theorem proven by Low, the Soft-Photon Approximations (SPA) [6–9] have been developed. The choice made for terms beyond the leading two orders introduces model dependence. This construction of the amplitude is not based on a microscopic model for the reaction dynamics.

In order to investigate the reaction dynamics in more detail, one performs microscopic calculations based upon a potential model. It has been a long-standing hope that the bremsstrahlung process will be able to discriminate between the different potential models. The first serious attempt to observe these differences was made in 1963 by Sobel and Cromer [10]. Already then, many of the ingredients which are necessary for the calculation of the bremsstrahlung process were introduced. It has been shown that once all the ingredients are included in the calculation of hard-photon production, the predictions of various modern potential models do not differ significantly, independent of whether they are finite range or energy dependent [11].

In proton-proton bremsstrahlung ($pp\gamma$), the first-order electric dipole transition is forbidden. Furthermore, the exchange of a single charged meson, to which a photon can couple, is not allowed. Due to the absence of these leading-order terms, the observables become more sensitive to other, more subtle, effects. The most important corrections to the leading order terms are the virtual Δ-isobar and the magnetic meson-exchange current [12–17]. The magnetic meson-exchange currents consist of an intermediate meson with quantum numbers $J^\pi = 1^-$ (ρ or ω) being transformed into a meson with quantum numbers $J^\pi = 0^-(\pi^0)$ thereby emitting a photon. Figure 1 shows the most important ingredients that enter in a microscopic calculation of the nucleon-nucleon bremsstrahlung process.

Other higher-order terms of the bremsstrahlung amplitude are due to negative-energy states which have been investigated by Martinus *et al.* [18]. This effect is only important at energies above the pion production threshold and does not contribute significantly at energies relevant for this work. The dependence of the electromagnetic $NN\gamma$ vertex on the off-shell invariant masses is a subject of investigation [19,20]. The extent to which this effect contributes is still under discussion. It should be noted that none of the effects mentioned can be observed individually. Independent of the theoretical description of the details of the process, the bremsstrahlung reaction is a different process from elastic

*Present address: National Superconducting Cyclotron Laboratory, Michigan State University, East Lansing, Michigan, 48824-1321 USA

†Corresponding author. Electronic address: nasser@kvi.nl

‡Present address: Universität Gießen, Heinrich-Buff-Ring 16, 35392 Gießen, Germany

 ©2004 The American Physical Society

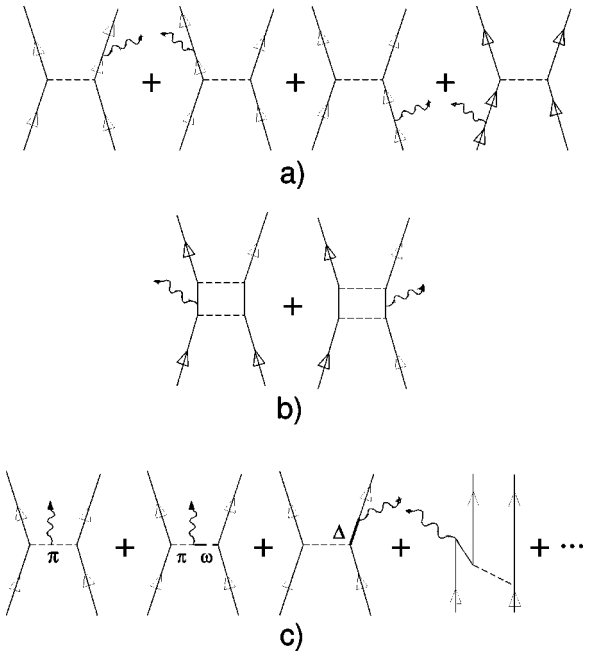

FIG. 1. The most important ingredients in a microscopic calculation. The top graphs represent the external bremsstrahlung contributions while the middle ones are for internal bremsstrahlung. The lower graphs show the higher-order effects discussed in the text. Note that in the $pp\gamma$ reaction, the contribution from the lower-left diagram is absent.

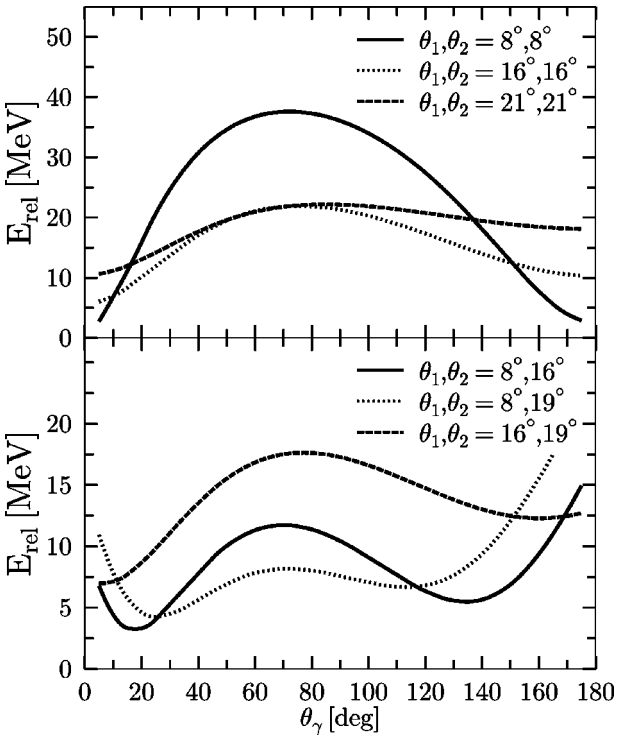

FIG. 2. The relative energy, as defined in the text, is shown as a function of the photon polar angle for various proton-angle combinations. The top (bottom) combinations are symmetric (asymmetric) proton angles.

scattering in that a photon vertex has been added and should be investigated both experimentally and theoretically. To show how different the bremsstrahlung process is from elastic scattering, one can look at the relative energy of the outgoing protons for various combinations of angles. This Lorentz-invariant variable, $E_{\rm rel}$, is defined here by $\sqrt{(E_1+E_2)^2-(\vec{p}_1+\vec{p}_2)^2-2M_p}$, where $E_1(\vec{p}_1)$ and $E_2(\vec{p}_2)$ are the energies (momenta) of protons 1 and 2, respectively, and M_p is the mass of the proton. In Fig. 2 this variable is shown as a function of the photon angle for small outgoing proton angles, and for an incoming-proton beam energy of 190 MeV. One clearly observes a very large range of relative energies for a fixed beam energy. For elastic scattering, the value of the relative energy is fixed at 95 MeV for all scattering angles. One can probe the nucleon-nucleon interaction at various energies by simply looking at a different region of the phase space. As can be observed in Fig. 2, one can probe very low relative energies of the outgoing protons. In this regime, one would expect another effect, namely that of the Coulomb force, to become important. Calculations performed to date [21–23] claim that the influence of this effect on the bremsstrahlung observables is minimal except for outgoing proton angles less than 6°. Incidentally, the variable $E_{\rm rel}$ is related to the energy of the photon in the c.m. frame, $E_\gamma^{\rm c.m.}$; this relation is expressed by the following equation:

$$E_\gamma^{\rm c.m.} = \frac{s-(E_{\rm rel}+2m_p)^2}{2\sqrt{s}}, \tag{1}$$

with $\sqrt{s}$ being the total energy of the system in the center of mass. $E_\gamma^{\rm c.m.}$ can be interpreted as a measure of how far the interacting nucleons are off their mass shell.

In order to go as far away as possible from the elastic-scattering channel, one needs to measure high-energy photons in a proton-proton bremsstrahlung experiment. Kinematics with high-energy photons restrict the protons to small scattering angles. At these angles the background due to the elastic-scattering channel is so large that it has hampered the experimental efforts in the past [24,25]. These experiments were not performed at small proton scattering angles and in addition the results suffered from low statistical accuracy. It was not until the eighties that the first high-luminosity experiment was performed at TRIUMF at small angles [26]. The experiment used a 280 MeV polarized proton beam, providing not only cross sections but also analyzing powers. However, the cross-section data from this experiment have been multiplied in the original paper with an arbitrary renormalization factor of two-thirds in order to obtain better agreement with theory. In addition, the experimental uncertainties are large compared to those in the data presented here. Another experiment at IUCF [27] has been performed, but a comparison with theory is difficult, due to the integration of the data over large parts of the phase space.

More recently other $pp\gamma$ experiments have been performed at small scattering angles [28–30]. The experiment with the accelerator COSY at Jülich [28] is a low-luminosity experiment with no photon detection system. The total number of collected events is about 1000. At Uppsala, a $pp\gamma$ experiment has been performed at 310 MeV [29], which is above the pion production threshold. Only a single proton and the photon are detected. The total number of collected events is about 60,000. The final data have not yet been

published, but the resulting accuracy will be similar to that of the TRIUMF data. At Osaka a $pp\gamma$ experiment at 400 MeV was performed [30] with two proton spectrographs and no photon detection system. The high resolution spectrographs allow an accurate determination of the photon momentum. However, such magnetic devices have small acceptances, resulting in a small coverage of the phase space.

In this paper, we report on the $pp\gamma$ cross-section and analyzing-power measurements performed at KVI with a beam energy of 190 MeV. The detection setup detects all three reaction products in coincidence. The total number of analyzed events is about 10 million. With this unprecedented accuracy, a detailed comparison with theoretical-model predictions is made possible. Results for some kinematics have already been published in Refs. [31–33]. Here, results for additional kinematical regions and a different way of presenting the data are discussed.

In Sec. II some of the details of the experimental setup will be discussed. Section III is devoted to the details of the data analysis. A description will be given of all the steps involved in going from the raw data to cross sections and analyzing powers. In Secs. IV A and IV B the results are presented along with results of some state-of-the-art calculations. Finally, in Sec. V we summarize this work. In the Appendix, some details concerning the kinematics and data tables are presented.

II. EXPERIMENTAL SETUP

As was mentioned before, the goal of the present measurements was to detect the protons at small laboratory angles. Furthermore, a measurement which aims to probe small effects should be performed with high accuracy. In order to obtain a high statistical accuracy, one has to maximize the luminosity, which is limited by the maximal count rate the setup can handle. In proton-proton bremsstrahlung, the predominant background process is elastic scattering. At the angles of interest the elastic-scattering yield is roughly a factor of 10^6 higher than the bremsstrahlung yield.

The experiments that are the subject of this work were performed with a 190 MeV polarized-proton beam [34] from the superconducting cyclotron AGOR [35] at KVI. The beam current was typically 6 nA with a typical polarization of ± 0.65. A liquid-hydrogen target cell with a thickness of 6 mm and a diameter of 20 mm was designed and used for these measurements [36]. The operational temperature of 15 K and pressure of 190 mbar were safely above the triple point. This way, the pressure exerted on the window would be minimal enabling the use of very thin windows. For the entrance and exit windows of the target, 4 μm-thick Aramid (from Toray, Japan) was used. This was the first time that such a thin window of synthetic material has been used in a beam of protons. These windows were used for extended periods of 2 to 3 weeks of beam on target without any visible damage.

For the detection of the outgoing protons, the Small-Angle Large-Acceptance Detector (SALAD), which was specifically designed and built for these experiments, was employed. It has a large solid angle of 400 msr and allows one to make cylindrically-symmetric measurements around the beam axis. The scattering angles covered range from 6° to 26°. The detector is segmented to handle high count rates and allows a hardware trigger rejection of protons stemming from elastic scattering. The design and operation of this detector is the subject of the first subsection. More detailed information can be found in Ref. [37].

In order to detect the bremsstrahlung photons, we have used the Two-Arm Photon Spectrometer, TAPS [38]. At KVI, TAPS consisted of approximately 400 BaF_2 crystals, which were used in two different geometries. In the first geometry, labeled as the "supercluster," all crystals were mounted at backward angles in a large hexagon, surrounding the beam pipe. This results in a polar angular range of $125° - 170°$ and a complete 2π azimuthal coverage. In order to investigate the angular distribution of the photons, a second experiment was performed where the cylindrical symmetry in photon detection was sacrificed. This second geometry, called the "block geometry," consists of six rectangular frames, each containing 64 crystals. These frames were positioned around the target on both sides of the beam pipe. TAPS covered more than 20% of the full 4π solid angle in both geometries. The TAPS detector is the subject of the second subsection. A description of the data acquisition and an overview of the triggers of both experiments are given in the third subsection.

A. The Small-Angle Large-Acceptance Detector

The Small-Angle Large-Acceptance Detector (SALAD) was used for the detection of the outgoing protons. It consists of two Multi-Wire Proportional Chambers (MWPC) for determination of the scattering angle of the outgoing protons [39]. Behind the two wire chambers, two layers of segmented plastic scintillators are mounted. The first layer is used for energy determination of the protons and is therefore called the "energy detector." Protons with an energy higher than 135 MeV will punch through the first layer and reach the second layer of scintillators called the "veto detector." These protons originate from elastic scattering and can be rejected via a hardware trigger [40]. Figure 3 shows a top view of SALAD, together with TAPS in the supercluster geometry.

The energy detector consists of 24 detection elements, 12 on the top side and 12 on the bottom side. The elements are placed in a cylindrical configuration, such that the contact plane between each two elements is in the same plane as the target center. This way, a particle moving in a straight line (not undergoing any interactions) will not fire more than one element. The material is BC-408, which is a fast scintillation plastic (2.1 ns decay time). The scintillators are read out with Philips XP 2282/B photo-multipliers (eight stages). These tubes are able to handle extremely high rates ($\approx$1 MHz).

Since protons stemming from elastic scattering must punch through the energy detector and protons from bremsstrahlung have to be stopped, the thickness of the energy detector has to be chosen with care. In Fig. 4 the range of protons in the material is plotted as a function of the kinetic energy (solid curve). This curve is obtained from the empiri-

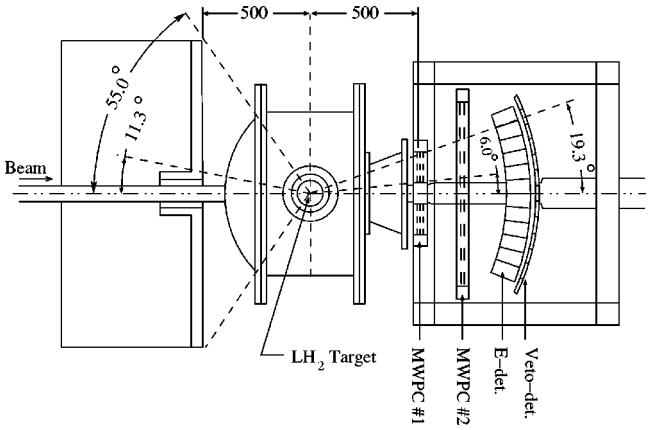

FIG. 3. Top view of SALAD (right) and the TAPS (left) detectors, configured in the supercluster geometry. The distances are given in mm.

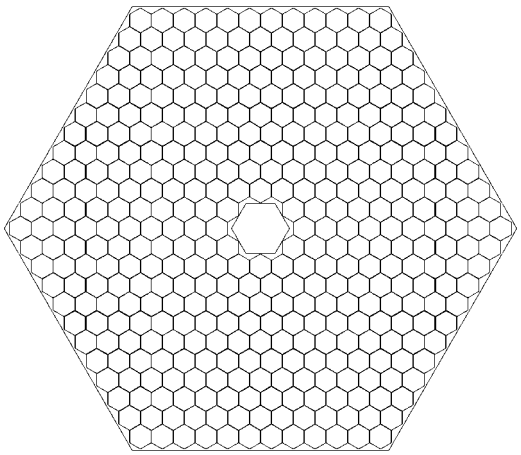

FIG. 5. The TAPS detector in the supercluster geometry, seen from the target. This setup contains 390 detection elements.

cal formula [41] for the range of charged particles in matter, R, as a function of their energy, E: $R=\alpha E^{1.75}$. The constant α depends upon the type of material and it has been obtained from a fit to a Monte Carlo simulation performed with GEANT [42]. The dashed-double-dotted curve shows the energy spectrum of protons originating from bremsstrahlung events with an incident beam energy of 190 MeV. The proton scattering angle is restricted to be between 5° and 28° and the photon scattering angle is restricted to be between 60° and 180°. These restrictions correspond roughly to the largest detection range of the employed setup. The dashed curve is the energy spectrum of protons originating from elastic scattering, where the proton scattering angle is restricted to the same range. Both spectra are the result of a Monte Carlo simulation where a phase-space distribution is taken. One can see that the two peaks are well separated. The high energy tail of the bremsstrahlung spectrum, however, has an overlap with the elastic spectrum. Evidently this part of the spectrum will be hardware rejected. These high energy protons correspond to a partner proton with a very low energy, which will anyways not be detected, due to the low-energy threshold of about 20 MeV in the SALAD detector. Note that the two spectra are not scaled to each other. The ratio of the real bremsstrahlung yield to the elastic-scattering yield is about 1 to 10^6. The thickness of the energy detector is chosen to be 11.25 cm corresponding to a punch through of protons with an energy larger than 135 MeV.

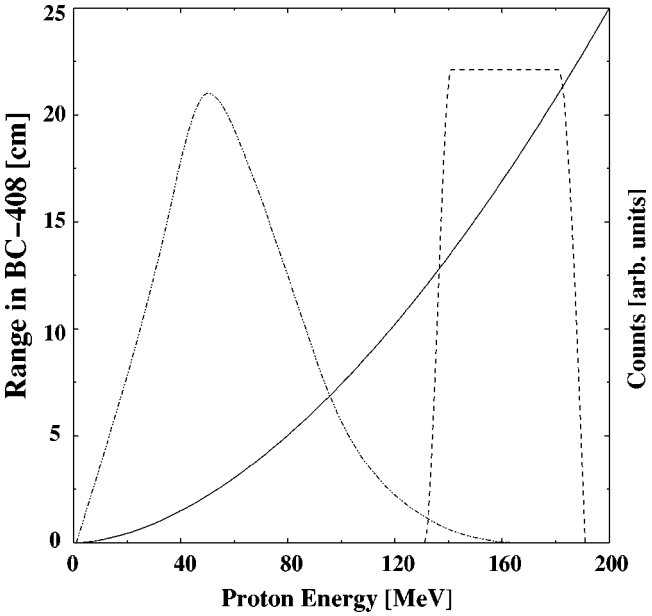

FIG. 4. The range of protons in plastic scintillator material (solid curve) and the proton energy spectra of $pp\gamma$ (dash-double-dotted curve) and elastic scattering (dashed curve).

The trigger is provided by the SALAD trigger module, which is described in detail in Ref. [40]. This CAMAC module is a programmable multiplicity unit, specifically designed for this experiment. It has the capability to select the $pp\gamma$ trigger condition on the SALAD side: $N_E - N_V \geqslant 2$ where $N_E(N_V)$ represents the total number of elements registering a particle in the energy (veto) detector. The module has four trigger outputs which can be programmed independently.

B. The two-arm photon spectrometer

In the supercluster geometry, the crystals are mounted in a large hexagon surrounding the beam pipe. The detector is placed at backward angles, such that the front face is at a distance of 50 cm upstream from the target. The polar angular range is 125° to 170° and the azimuthal scattering angular range covered is complete for nearly all scattering angles. In Fig. 5 the supercluster geometry of TAPS is depicted, as seen from the target. The outer two rings of BaF_2 crystals were equipped with plastic elements making these elements phoswich detectors. These elements have a 15 mm thick plastic scintillator mounted in front of the BaF_2. The light produced by the plastic element is detected with the same phototube as the light of the BaF_2. This was done to discriminate photons from protons and leptons via a pulse-shape analysis. The choice for phoswich detectors, however, turned out to be problematic for the trigger, since their count rate was more than a factor 5 higher than that of a normal BaF_2 detector. This is due to the fact that the plastic detectors deliver a fast high amplitude pulse. This causes the Leading-

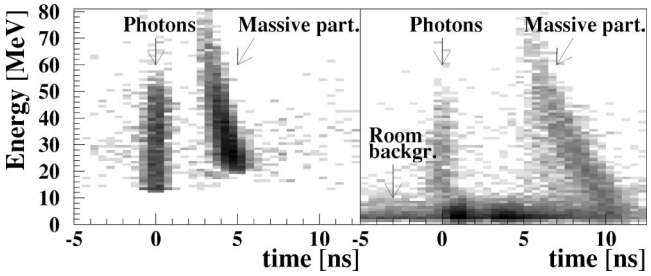

FIG. 6. The Energy versus the time-of-flight for a normal BaF_2 crystal (left panel) and for a BaF_2 crystal equipped with a plastic detector (right panel). Events have been selected where the LED-high has fired.

Edge Discriminator (LED) to fire even when very low-energy particles, which hardly contribute to the total charge of the pulse, enter the detector. This can be seen from Fig. 6, where the energy is plotted versus the time-of-flight of the particle relative to the rf of the cyclotron for events observed using a normal BaF_2-crystal and using a BaF_2 equipped with a phoswich detection element. Events have been selected where a LED, which was set to a 15 MeV threshold, has fired. One can observe two bands in the left panel. The vertical band consists of photons, which have times-of-flight independent of their energy. The curved band consists of massive particles, e.g., protons produced in the target foils, whose times-of-flight are longer when their energies are lower. This band in the phoswich detector extends much further to lower energies than it does in the normal detector. Furthermore, in the phoswich detector one can observe a band with low-energy particles, which are not time-correlated with the beam. These particles originate from the room background, and fire the LED of the detectors equipped with phoswiches. Increasing the LED-high threshold of the phoswich detectors in order to decrease their count rate, would render them useless for low-energy photon detection. One detail in Fig. 6 is that the massive-particle band and photon band are more separated in time in the phoswich detector. This is explained by the fact that this detector was mounted at a larger distance from the target.

In the second experiment, referred to as the "block geometry," the crystals are mounted in six blocks each containing 64 BaF_2 crystals. In front of each crystal a plastic NE102A scintillator is mounted, which allows for a distinction between charged and neutral particles [43]. These plastic scintillators are read out with separate phototubes. This configuration is depicted in Fig. 7. The six blocks are positioned around the target at a distance of approximately 66 cm. The angular range is $60°-170°$.

In both geometries, the analog signal from a BaF_2 module is connected to a QDC (charge-to-digital-converter), where the signal is integrated twice, allowing particle identification via pulse-shape analysis. The original signal is discriminated three times. The CFD (constant-fraction-discriminator) signal which was created with a threshold setting of 500 keV, is used for measuring the timing with respect to the rf of the cyclotron. This timing is thus a measure of the time-of-flight of incident particles. Furthermore, the CFD signals are used to define the individual integration gates of the QDCs. Two

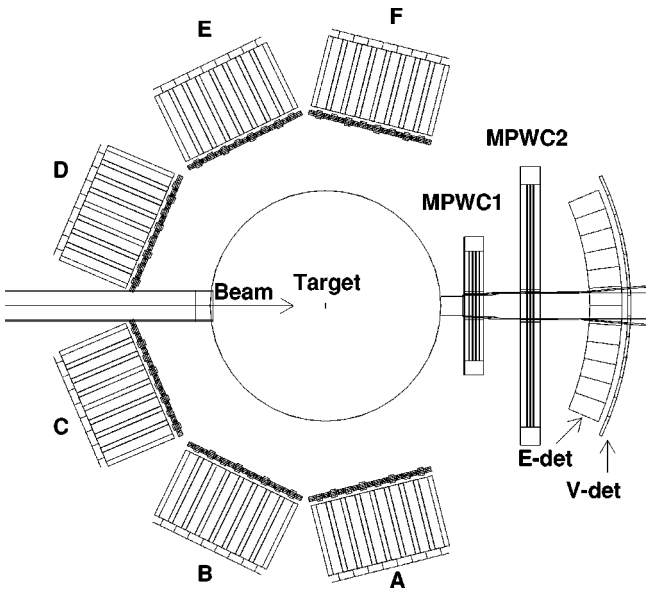

FIG. 7. Top view of the SALAD and TAPS detectors in the block geometry (labeled A–F). This setup contains 384 BaF_2 detection elements.

leading edge discriminator (LED) signals, called LED-high and LED-low, are used in the trigger logic. The level of the LED-high was set to 15 MeV in both experiments. The effect of this cut is depicted in Fig. 8.

In the supercluster geometry an OR of all LED-high signals was used as a TAPS trigger to provide the strobe for the SALAD-trigger box. In the block geometry where the charged-particle vetos (CPVs) were available, charged particles were vetoed by an anti-coincidence of the LED signals from the CPV with the corresponding BaF_2 LED-low signals using multiplicity pattern units (MPU). A Quasi-Neutral

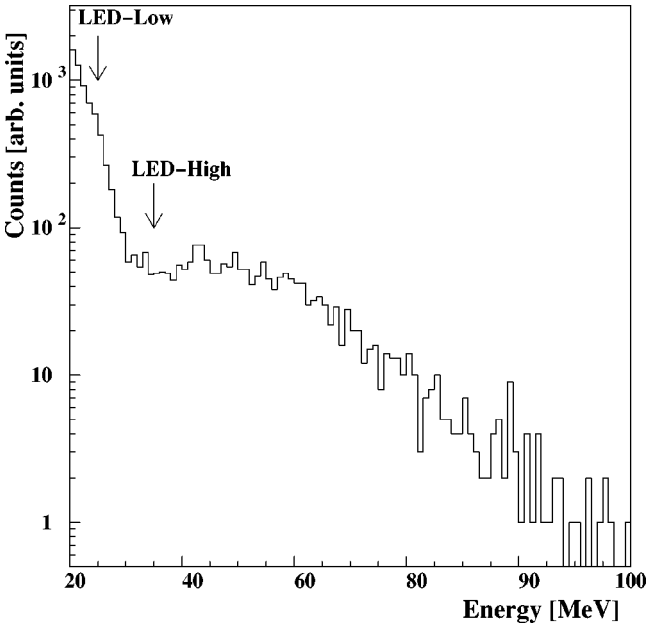

FIG. 8. Energy spectrum of the TAPS detector. The levels of the two LED triggers are indicated.

TABLE I. A sample list of triggers used in the supercluster experiment and their rates at 6.5 nA nominal beam current. The live-time of the data-acquisition system was 58% at this current. DS stands for down-scale factor. The column Raw indicates the raw rate of the trigger and the column ACQ indicates the rate with which the data-acquisition system wrote to tape.

Trigger	Description	DS	Raw	ACQ
		^{2}log	(kHz)	(Hz)
CFD	CFD OR BaF_2	15	719	13
LEDLo	LED-low OR BaF_2	11	103	30
LEDHi	LED-high OR BaF_2	8	12	28
$pp\gamma$	$N_E - N_V \geqslant 2$ and LEDHi	0	0.85	499
min bias	CFD or SALAD and LEDHi	8	9.6	22
$p\gamma$	$N_E - N_V \geqslant 1$ and LEDHi	7	3.6	4
RF	RF / 225×10^3	0	0.27	177

(QN) trigger was obtained by making a block-wise AND of a LED-high signal with the output of the MPU. The LED-low was set to 5 MeV in the block geometry and was used in the more complex dilepton trigger via MPU and memory-lookup units.

C. Data acquisition

The data were stored on digital linear tapes (DLTs) by the TAPS data acquisition. The CAMAC-crate controllers from TAPS are chained via a VME subsystem bus and are connected by a VME-based microprocessor to the data-acquisition computer. The data from SALAD were passed to VME-based dual-port memory units (LeCroy DPM 1190), one for the scintillator information (TDC and FERA) and one for the wire-chamber data (PCOSIII). The data handling rate is about 300 kB/s, resulting in approximately 800 events/s. A fraction of the events were passed via Ethernet to the on-line data analysis.

The triggers of the supercluster experiment are listed in Table I. The most important trigger is the $pp\gamma$-trigger. Also, the heavily down-scaled rf of the cyclotron is used as a trigger by reading out all the detectors once every 225×10^3 beam pulses. This trigger is used for the determination of the elastic cross section, which in turn is used for the absolute normalization of the $pp\gamma$ data. The raw rate is the rate at which the trigger fires and the data-acquisition rate is the rate at which this trigger was written to tape.

The triggers and their rates for the block-geometry experiment are listed in Table II. In this geometry the two forward TAPS-blocks A and F (see Fig. 7), receive a large contribution of elastically-scattered protons which penetrate into the BaF_2 crystals. Consequently, in these blocks more than 80% of all LED-high triggers originate from these protons. Therefore, the rate of the QN trigger was very much different from the rate of the LED-high trigger in these blocks. This is different from the situation in the four backward blocks, where the rate of the QN trigger is approximately the same as the rate of the LED-high trigger. For optimization of the trigger rates, a pseudo-neutral (PN) trigger was made consisting of an OR between the LED-high of the four backward blocks and the QN trigger of the two forward blocks. The trigger from the TAPS side was, therefore, the PN trigger.

TABLE II. A sample list of triggers used in the block experiment and their rates at 6.5 nA nominal beam current. The live-time of the data-acquisition system is 53% at this current. See Table I for the abbreviations.

Trigger	Description	DS	Raw	ACQ
		^{2}log	(kHz)	(Hz)
CFD	CFD OR BaF_2	15	974	15
LEDLo	LED-low OR BaF_2	11	205	52
LEDHi	LED-high OR BaF_2	8	35	71
VETO	OR of the CPV	13	819	53
QN	LEDHi with VETO	∞	8.8	0
PN	QN A/F, LEDHi B-E	∞	9.9	0
$pp\gamma$	$N_E - N_V \geqslant 2$ and PN	0	0.92	494
$pp\gamma$ no PN	$N_E - N_V \geqslant 2$ and LEDHi	7	7.2	56
min. bias	SALAD-OR and PN	7	9.5	39
$p\gamma$	$N_E - N_V \geqslant 1$ and PN	6	3.5	29
RF	RF / 225×10^3	1	0.27	66

III. DATA REDUCTION AND ANALYSIS

In this section, the procedure used to obtain the bremsstrahlung observables is described. A discussion is given of the elastic channel, which is responsible for the background events recorded to tape, but which is also used for the determination of the luminosity. The bremsstrahlung channel is analyzed in two steps: First a pre-selection of $pp\gamma$ candidates is made, which is followed by an analysis of the kinematics to select the real $pp\gamma$ events. In the last subsection we discuss the various efficiencies which enter in the determination of the cross section.

In order to compare the theoretical predictions for the cross section with the experimental data, one needs an expression for this observable in terms of experimental quantities. For a scattering experiment on a target at rest one can derive the relation between the number of observed events N_{det} and the cross section:

$$\left(\frac{d\sigma}{d\mathcal{F}}\right)_{meas} = \frac{1}{\delta\mathcal{F}} \frac{A_{target}}{\epsilon_{det} n_{inc} \rho_{target} \delta x N_A} N_{det}. \qquad (2)$$

Here, $\mathcal{F}$ stands for any choice of coordinates and δF is the size of the experimental bin in these coordinates. The number of incoming particles is n_{inc}, ρ_{target} is the mass density of the target, δx is the target thickness, N_A is Avogadro's number, A_{target} is the mass number of the target atoms, and ϵ_{det} is the detection efficiency.

A. Estimation of the background

The predominant background process in $pp\gamma$ measurements is proton-proton elastic scattering. Via a Monte Carlo simulation one can estimate the background trigger rate due

TABLE III. The probability for the different track scenarios of elastic protons in SALAD at an incident energy of 190 MeV.

Case	N_E	N_V	Prob. (%) (GEANT)	Prob. (%) (Data)
–	1	1	77	77
1	1	0	17	14
2	2	0	3	4
3	2	1	3	5

to this process. At the incident energy of 190 MeV, the kinematics of elastic scattering can be regarded as nonrelativistic, in which case the opening angle of the two protons is always 90°. The maximum opening angle subtended by SALAD is 52°, therefore only one of the two protons of an elastic scattering event is able to reach SALAD. This was a very important consideration in the design of the detector, since the $pp\gamma$-trigger requires a coincidence of two protons in SALAD.

The trigger condition on the SALAD side is $N_E - N_V \geqslant 2$. When one elastically-scattered proton traverses SALAD, it will normally fire one element in the energy detector and one element in the veto detector, implying that $N_E - N_V = 0$. Two or more elastically-scattered protons traversing SALAD will not change this condition. However, there are three other possibilities of importance which can spoil this scenario.

(1) (p,n) *reaction*. A proton can collide with a nucleus in the energy detector and produce a neutron, for example, via knock-out or charge-exchange reactions. The residual proton energy (if any) may not be enough to reach the veto detector, while the neutron may escape without deposit energy. In this case $N_E - N_V = 1$.

(2) (p,p) *reaction*. A proton can scatter off a nucleus in the energy detector. The new direction of the proton may be such that it fires two neighboring energy detector elements and no veto element. In this case $N_E - N_V = 2$.

(3) *Crossover*. Due to straggling, a proton can cross over from one energy detection element to the other, and fire one veto element. In this case $N_E - N_V = 1$.

A random coincidence between situations (1) and (1), (3) and (3), and (1) and (3) will produce a valid $pp\gamma$ trigger on the SALAD side. Situation (2) produces the $pp\gamma$ trigger with only one proton. In Table III the probability for each track scenario is shown as simulated with GEANT [42] and as found in the data. In order to make a fair comparison with the data, the GEANT tracks are selected on the number of detector elements they fire, and not on the interaction mechanism. The agreement between the simulation and the data is rather good, taking into account the systematic errors on the hadronic interactions in GEANT.

Given the probability for the occurrence of the tracks, one can estimate the rate of the $pp\gamma$ trigger, starting from the single rates of the SALAD and TAPS detectors. In Fig. 9 the two components of the predicted $pp\gamma$ rate are plotted as a function of the beam current. The first component (dash-dotted line) consists of an elastic-scattering track where $N_E = 2$ and $N_V = 0$ (case 2 above) in random time coincidence with a TAPS-trigger. The second component (dotted line) consists of two random tracks in SALAD delivering each $N_E - N_V = 1$ (cases 1 and 3 above) in random time coincidence with a TAPS-trigger. The total $pp\gamma$-trigger rate (solid line) is the sum of these two rates. It can be seen that this rate is in very good agreement with the observed trigger rate (diamonds). At a beam current of about 5 nA, the real $pp\gamma$ rate was about 8 counts/s.

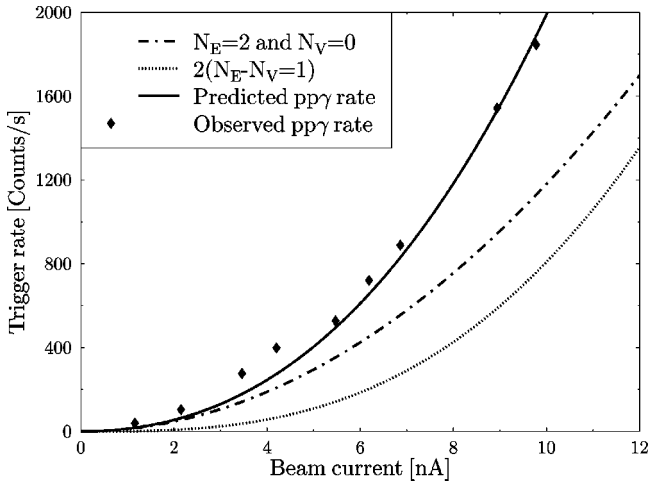

FIG. 9. The observed $pp\gamma$-trigger rate as a function of beam current along with the predicted rate.

B. The elastic proton-proton channel

The accuracy of an absolute cross section measurement does not depend only on the statistics of the measurement, but also on the systematic uncertainty in determining the integrated luminosity. The latter is defined as the product of n_{inc} and the areal density of the target, $\rho_{target}\delta x$. A direct measurement of n_{inc} is performed by measuring the integrated current with a Faraday cup in the beam stop. For the present setup, this method contributes with a 3% systematic uncertainty, but the relative accuracy is better than 1%. The areal density of the target is the product of the mass density of liquid hydrogen at the triple point ($\rho = 70.8$ mg/cm^3) and the thickness of the target cell, $\delta x = 6$ mm. These values result in the *nominal* areal density: 42.5 mg/cm^2. However, since the pressure difference over the synthetic target windows is large, the target is subject to bulging. The variations in bulging, which are dependent on many factors, compromise a precise determination of δx. Since the *direct* determination of the luminosity is not possible to the level of precision aimed for, it was decided to use the elastic proton-proton scattering cross section instead. The differential cross section for this process is known to a high accuracy from various phase-shift analyses of the *pp* world data-set [1,44]. The luminosity is obtained by fitting the measured *pp* angular distribution to the theoretical predictions, with only the luminosity as a free parameter.

A similar method is used for determining the beam polarization. The dependence of the cross section on the azimuthal angle ϕ is described by

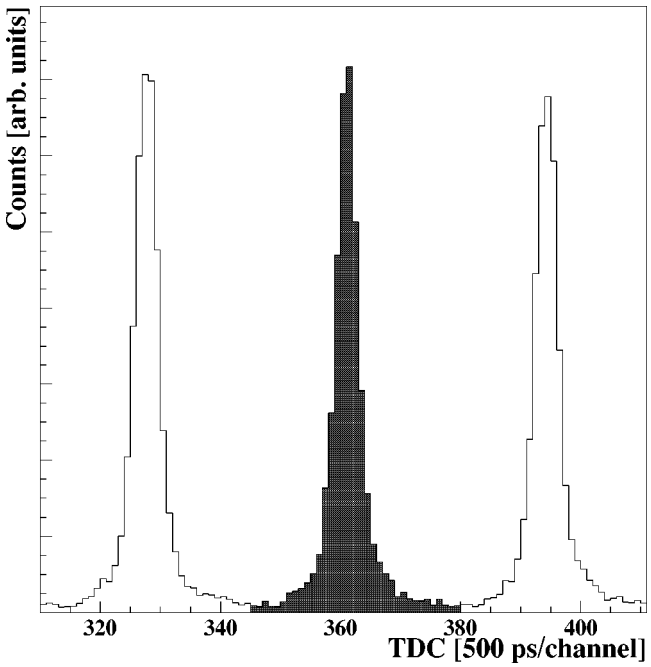

FIG. 10. The TDC spectrum of one SALAD energy scintillator. Events have been selected originating from the rf-trigger. The filled part of the spectrum indicates the part used to produce the elastic-scattering cross sections and analyzing powers.

$$\frac{d\sigma^{pol}}{d\Omega} = \frac{d\sigma^{0}}{d\Omega}(1 + p_y A_y \cos\,\phi). \tag{3}$$

By fitting the elastic proton-proton distribution to this expression, taking A_y from a phase-shift analysis, one obtains the beam polarization p_y.

The elastic-scattering information is obtained from a down-scaled "singles" measurement as follows. AGOR delivers a pulsed 190 MeV proton beam with a frequency of 60 MHz. The 60 MHz signal from the cyclotron is down-scaled by a factor of 2.25×10^5, resulting in a 267 Hz signal, which is used as the rf trigger. A rf trigger forces a read out of all detectors whether or not a reaction has taken place. However, with the luminosity chosen for the $pp\gamma$ experiment, the chance of finding an elastic event within this trigger is rather high.

In this analysis the assumption is made that the only two processes delivering particles in SALAD are elastic proton-proton scattering and proton-nucleus scattering in the target foils. The contribution of other processes, like bremsstrahlung, is less than 10^{-3} and therefore neglected. The background from the target windows is determined via an independent measurement with an empty target cell. In Fig. 10 the TDC spectrum of the SALAD energy scintillators is shown for events originating from the rf trigger. In this spectrum one can clearly see the pulsed structure of the beam. A time gate is set around one of the rf peaks, which ensures that the luminosity per beam pulse is measured. This gate is indicated with the dark area in Fig. 10. The events which lie within the specified time range are then analyzed for tracks. A track in SALAD consists of one hit in the wire-chamber (providing θ and ϕ information) and at least one (and possibly more) energy detector element(s). The track, as determined by the MWPC information has to point to the position of the corresponding element in the energy detector giving a signal. An energy element, which has fired with no wire-chamber hit pointing to its position, is rejected since the kinematics of those events cannot be determined. To correct for these rejected events one has to fold the measured distribution with the wire-chamber efficiency. In the case when two adjacent energy elements fire, this means that a proton has crossed over from one element to another, either due to multiple scattering or a hadronic interaction. The presence of a signal from a veto detector element is not taken into account in this analysis, since not all elastically-scattered protons reach the veto detector.

TABLE IV. The results of fitting the elastic-scattering data to the two phase-shift analyses PWA93 and SAID. Ndf stands for "Number of Degrees of Freedom." In the case of the cross section, the data are integrated over ϕ, resulting in a relatively low number of data points for the luminosity fit. This is in contrast with the fit to the analyzing powers, where the data are binned both in θ and in ϕ. LCF stands for the luminosity correction factor.

		PWA93		SAID	
Fit	Ndf	Value	χ^2	Value	χ^2
LCF	8	0.871 ± 0.002	0.36	0.869 ± 0.002	0.88
p_y(WF)	83	-0.724 ± 0.026	0.91	-0.720 ± 0.026	0.91
p_y(SF)	83	0.521 ± 0.026	0.98	0.517 ± 0.026	0.98

The kinematics of an elastic scattering event is completely determined by the polar (θ) and azimuthal (ϕ) angles of the detected proton. The data are binned in these two parameters and the differential cross section is determined via Eq. (2), using the nominal luminosity. This analysis is performed for two subsequent runs: in the first run, the normal liquid-hydrogen target was used and in the subsequent run, the hydrogen was removed from the target, but the foils were kept in the cryogenic state. The background corrected spectrum is obtained by subtracting the nominal cross sections of these two runs. At the most forward angles in SALAD (7°), the background from the foils amounts to 12%, while it decreases rapidly at larger scattering angles. Beyond 15°, the background is generally less than 3%. Therefore, only the data for angles larger than 15° were used in comparison with the theoretical predictions. The wire-chamber efficiency is determined from the run with a liquid-hydrogen target and corrected for. The full coverage of the azimuthal angle, ϕ, results in a higher statistical accuracy for the differential cross sections and the analyzing powers. The correction factor to bring the luminosity from its nominal value to the actual value is obtained by comparing the measured cross sections as a function of θ to the predictions from two phase-shift analyses: SAID [44], developed at the Virginia Polytechnic Institute and PWA93 [1], developed at the university of Nijmegen. The results of these fits are listed in Table IV. The luminosity correction factors listed here originate primarily from the known bulging in the target. From the reduced χ^2 values, one can conclude that the data are in excellent

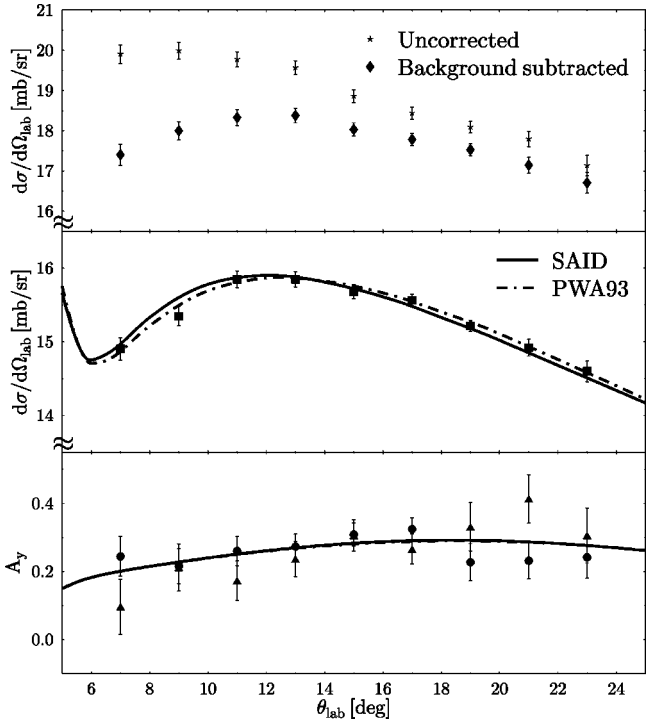

FIG. 11. The elastic-scattering cross sections and analyzing powers as a function of θ. The normalizations of the cross section and the beam polarization are fitted to two different phase-shift analyses (see the text). Note that the *y*-axis of the cross section does not start at zero. The top panel shows the cross section using the nominal luminosity with and without the correction for contributions from the target foils. The middle panel compares the normalized, efficiency corrected, angular-distribution data with phase-shift analyses. The lower panel shows the same distribution for the analyzing power, where the two data symbols refer to the two states of the beam polarization.

agreement with the predictions from the phase-shift analyses. In the middle panel of Fig. 11, the renormalized data are shown along with the predictions from SAID and PWA93.

In order to obtain the beam polarization, one has to investigate the azimuthal distribution [see Eq. (3)]. During the experiment, the beam polarization is periodically changed between three different polarization states. This is achieved by switching the polarized-ion source of the cyclotron to the Weak-Field (WF) state, the Strong-Field (SF) state and the field-OFF (OFF) state. To correct for imperfections in the detector geometry and the beam optics, the data are corrected with data taken with the source in the OFF state:

$$I(\theta,\phi) = \frac{\sigma^{\uparrow}_{LH2}(\theta,\phi) - \sigma^{\uparrow}_{emp}(\theta,\phi)}{\sigma^{0}_{LH2}(\theta,\phi) - \sigma^{0}_{emp}(\theta,\phi)} \tag{4}$$

$$= 1 + p_y A_y^{pp}(\theta)\cos\,\phi. \tag{5}$$

Here, $\sigma^{\uparrow}$ stands for the cross section measured with the polarized source either in the WF or SF state and σ^0 is the cross section measured with the source in the OFF state. The subscripts *LH*2 and *emp* stand for liquid-hydrogen and empty target, respectively. The distribution I is fitted by Eq. (5), which is easily derived from Eq. (3), with the beam polarization p_y as the only free parameter. For the analyzing powers $A_y^{pp}(\theta)$, the predictions of the SAID and PWA93 analyses are taken. The results of the fits are also listed in Table IV. Using the thus-obtained beam polarizations for the WF and SF states of the polarized source, one can extract the analyzing powers from the data. These are depicted in the bottom panel of Fig. 11. It is clear that the agreement between data and theory is excellent.

C. The bremsstrahlung channel

The data-set of the $pp\gamma$ supercluster experiment comprises a total of 180 GB, and the data of the $pp\gamma$ block-geometry experiment 400 GB. Since quick and repeated analysis of this very large amount of data is not feasible and most of the data consist of background events, a pre-selection of $pp\gamma$ candidates is made in an off-line analysis. This pre-selection is based on time-of-flight (TOF) information from TAPS. From Fig. 6, one can see that the TDC-spectrum of the BaF_2 crystals consists of two distinct peaks, one corresponding to photons and one to massive particles. The time spectra of the BaF_2 crystals are calibrated such that the photon peak has its centroid around zero. A photon is identified with a gate ranging from −2 to 2 ns. Furthermore, a condition is set on the total energy of the photon cluster, defined as the sum of the energies deposited in all neighboring TAPS detector elements in the event. A low energy threshold of 20 MeV was required on photon cluster energy. This latter cut provides the rejection of the room background (see the right panel of Fig. 6). New event files are made, where only events are stored which satisfy the two cuts just mentioned. No cuts on the SALAD side are made at this point. This reduces the total data-set by roughly a factor of 10 for both experiments. This reduction is sufficient to store the data of one experiment on a single tape.

Having pre-sorted the data, the bremsstrahlung events are extracted from the pre-sorted event files. The first step in the analysis on the SALAD side is to determine the proton tracks. This is done in a similar way as with the selection of the elastic events. A track thus consists of a wire-chamber hit (providing θ and ϕ) and a signal from at least one energy detector. The only difference from the data analysis of the elastic-scattering channel is that no veto detector behind an energy scintillator is allowed to have fired. If a veto detector did fire, the proton originated from an elastic interaction. A proton track in SALAD provides the two angles θ and ϕ and the energy deposited in the scintillator. On the TAPS side, the crystals which fired are grouped in clusters. A cluster provides the same information for the photon (θ, ϕ and energy deposit) as a track in SALAD does for a proton. A large part of the background events originates from one proton (see Table III), and will thus produce one track in SALAD. These events clearly do not qualify as $pp\gamma$ candidates.

After the tracks in SALAD and clusters in TAPS have been identified, the $pp\gamma$ kinematics are reconstructed. Starting with the scattering angles of the protons and the polar angle of the photon (θ_1, ϕ_1, θ_2, ϕ_2, θ_γ), the analysis attempts

TABLE V. Selections and their effect on the data for a typical run of both experiments. The beam current was ≈5 nA in both cases.

	Supercluster		Block	
Selection	Perc.	Factor	Perc.	Factor
Recorded to tape	100%	–	100%	–
$pp\gamma$ trigger	53.7%	1.9	55.7%	1.8
TOF & $E_\gamma \geqslant 20$ MeV	4.9%	10.0	5.7%	9.6
$\geqslant 2$ tracks in SALAD	2.3%	2.1	2.2%	2.6
Kinematically allowed	2.1%	1.1	2.0%	1.1

to reconstruct the energies of the three particles and the azimuthal angle of the photon (E_1, E_2, E_γ and ϕ_γ). In Appendix A the kinematics and the procedure followed for the reconstruction are described. For background events, however, one may not be able to solve Eq. (A9), since it may not have a real-number solution for a random combination of θ_1, θ_2, ϕ_1, ϕ_2 and θ_γ. In Table V the first series of selections applied to the data are listed, together with the number of events which survives these cuts.

The sample of events with which Eq. (A9) was successfully solved is used for further inspection. This inspection is performed by comparing the reconstructed kinematical variables (E_1, E_2, E_γ and ϕ_γ) with their measured counterparts. Figure 12 consists of four scatter-plots of the measured and reconstructed energies of the particles belonging to the events subjected only to the above-mentioned selections. The

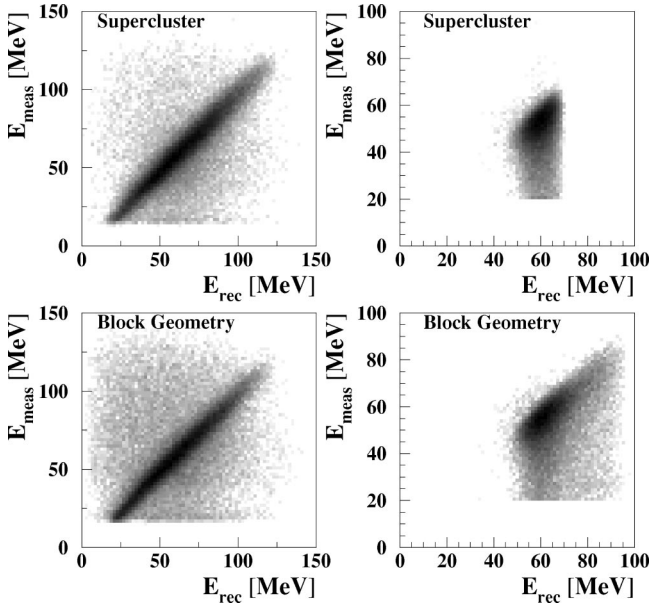

FIG. 12. Measured versus reconstructed energy of the protons (left panel) and the photon (right panel) for all events, where kinematics could be solved. The gray scale indicating the number of events is logarithmic in order to enhance the areas with a low number of events. It is clear that the spectra are dominated by $pp\gamma$ events, since reconstructed energies are equal to measured ones. However, some background is still present.

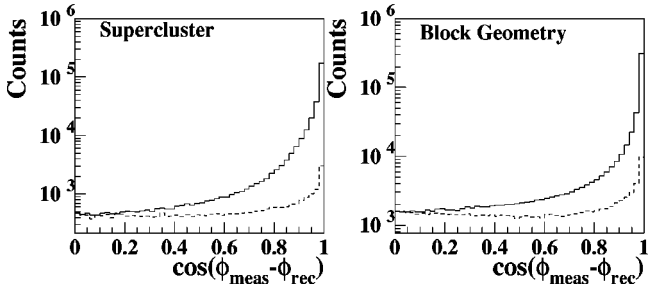

FIG. 13. The distribution of $\cos(\phi_{\gamma,\mathrm{meas}} - \phi_{\gamma,\mathrm{rec}})$ is shown for the range 0 to 1 as the solid line. For the range between −1 and 0, the results have been mirrored around 0 (dashed line) in order to show the shape of the background (see the text).

left panels depict the correlation between the reconstructed and measured proton energies for the supercluster- and block-geometry experiments. Since a $pp\gamma$ event has two protons, each event has two entries in these plots. In the right panel, the same plots are made for the photon energy. It is clear that the spectra are dominated by $pp\gamma$ events. However, some background still remains. This background is largely removed by making use of the over-determined kinematics, i.e., setting conditions on the spectra shown in Fig. 12, and on ϕ_γ (Fig. 13).

The azimuthal angle of the photon, ϕ_γ, is the most accurate overdetermined kinematical variable. In Fig. 13, the solid curves show the distribution of $\cos(\phi_{\gamma,meas} - \phi_{\gamma,rec})$. This trigonometric representation is used to remove the cyclic nature of the azimuthal angle (359° is close to 0°). For real $pp\gamma$ events, this variable is close to 1. For background events, no correlation exists between the measured and reconstructed ϕ_γ. From this assumption, immediately follows that the cosine distribution for background events is an even function. The dashed curves in Fig. 13 are the part of the spectrum where $\cos(\phi_{\gamma,meas} - \phi_{\gamma,rec})$ is negative (the absolute value is plotted). This part of the spectrum consists of events in which the measured azimuthal angle of the photon is more than 90° *away* from its reconstructed value. These events are considered background events. Because the background contribution of the spectrum is an even function, the dashed lines thus show the magnitude of the background residing under the $pp\gamma$ peak. From the assumption of no correlation between ϕ_{meas} and ϕ_{rec}, one can show that the background contribution is proportional to $1/\sqrt{1 - \cos^2(\phi_{meas} - \phi_{rec})}$, which is in very good agreement with the observed shape of the background. From Fig. 13, one can conclude that all the true bremsstrahlung events obey the condition $\cos(\phi_{\gamma,meas} - \phi_{\gamma,rec}) > 0.2$, since it is there that the solid and dashed curves start to deviate from each other.

In Fig. 14 the differences in reconstructed and measured energies of proton 2 is plotted versus that of proton 1. The cut $\cos(\phi_{\gamma,meas} - \phi_{\gamma,rec}) > 0.2$ is made for the plots in the left panel. All bremsstrahlung events survive this cut. In the right panel, the remaining events, consisting of background only, are plotted. For the background events, no clear correlation between the measured and reconstructed values of the proton

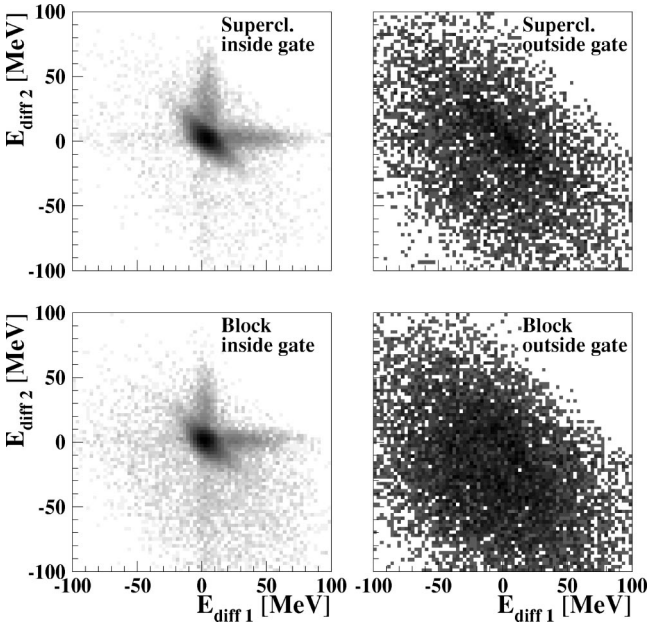

FIG. 14. The difference between measured and reconstructed energies for proton 2 versus that of proton 1; $E_{\mathrm{diff}}=E_{\mathrm{rec}}-E_{\mathrm{meas}}$. The left panels show the bremsstrahlung events. The plots in the right panels consist entirely of background events. The gray scale indicating the amount of events is logarithmic.

energies is present. In the plots containing the bremsstrahlung events, one can observe a concentration of events around the origin, with small tails along the diagonal. In addition to this, one can see two other bands, one along the positive *x*-axis and one along the positive *y*-axis. These are events where one of the protons had a hadronic interaction. In this case a part of the energy of the proton is not measured, resulting in a too-low measured energy. Also, along the negative *x*- and *y*-axes one can observe much fainter bands. These are pile-up events, where another particle is detected along with a valid $pp\gamma$-proton in the same scintillator, resulting in a too-high measured energy. One can also see that the background is not completely removed. The maximum level of background is about 5% depending on the kinematics.

In order to obtain cross sections and analyzing powers from the data, events are selected with $\cos(\phi_{\gamma,meas}-\phi_{\gamma,rec})>0.2$. In order to correct for the remaining background, also events with $\cos(\phi_{\gamma,meas}-\phi_{\gamma,rec})<-0.2$ are selected and subtracted from the first set of events. This procedure is slightly different from the procedure described in Ref. [31], where $\cos(\phi_{\gamma,meas}-\phi_{\gamma,rec})>0.3$ was chosen and no background subtraction was performed. The background residing under the $pp\gamma$ peak is less than 1% for the specific kinematics shown in that publication.

D. The efficiencies of the measurement

In order to obtain absolute cross sections, one has to know the efficiency of the measurement. In every step in the selection of true $pp\gamma$ events, starting from the detectors and the trigger, and up to software analysis of events, one might throw away good events. The parameter ϵ in Eq. (2) accounts for this effect and it is the product of all individual efficiencies encountered in each of the steps in determining the good $pp\gamma$ events. These steps are listed in Table V and will be discussed in reversed order. The efficiency of the kinematics reconstruction algorithm is 100%.

The efficiency of the track reconstruction in SALAD is solely dependent on the wire-chamber efficiency, since the efficiency of plastic scintillators is generally known to be 100%. The efficiency of each MWPC1 plane is measured via selecting single tracks in the two other planes and the scintillators. Subsequently, one can check for the presence of the first plane. The efficiency of the MWPC2 planes are checked in the same way with the additional use of the *u*-plane of MWPC1. This position-dependent efficiency has to be applied twice, since a wire-chamber hit is required for both protons. A more detailed description of the performance of the wire chambers can be found in Ref. [39].

The two cuts made in TAPS (TOF and $E_\gamma \geqslant 20$ MeV) might throw away good events. Due to the generosity of the cut in TOF, ranging from −2 to 2 ns, no photons are cut away. The effect of the cut of $E_\gamma \geqslant 20$ MeV needs to be investigated. This was done with the help of GEANT simulations in which the detector response was examined with the cut set at 20 MeV. The energy of the photons for the present geometries is around 60 MeV and the effect of the energy cut of 20 MeV is only present due to edge effects in TAPS. If a photon hits a BaF_2 detector which is positioned at the edge, a part of the electromagnetic shower might escape and not be detected. Simulations show that the net effect of the cut of $E_\gamma \geqslant 20$ MeV is that approximately 3% of the bremsstrahlung events are cut away, depending on the kinematics. This has subsequently been corrected for.

The azimuthal acceptance in the block geometry is dependent on θ_γ, which is a pure geometrical effect, and on the photon energy, due to the 20 MeV cut. Also in the supercluster geometry, the azimuthal acceptance is not complete at the edge of the detector. Strictly, the azimuthal acceptance is not an efficiency, but a part of the solid angle, denoted as $\delta\mathcal{F}$ in Eq. (2). In the choice of coordinates relevant for this work, the dependence on ϕ_γ is implicit, making an analytical determination of $\delta\Omega_1\delta\Omega_2\delta\theta_\gamma$ practically impossible. This problem is circumvented by integrating the data over ϕ_{event} (see Fig. 23 later) and implementing the ϕ_γ-acceptance as an efficiency, determined with GEANT [42]. In the simulations, $pp\gamma$ events are generated according to phase-space distribution. The generated events provide the "true" photon distribution, corresponding to an integration over those proton angles covered by SALAD, where the azimuthal coverage is complete. The photons are tracked through the setup, providing a simulation of the measured photon distribution. By dividing these two distributions, one obtains, for a certain bin in θ_γ, the combined efficiency for the azimuthal acceptance and the $E_\gamma \geqslant 20$ MeV cut.

The trigger efficiency is defined as the efficiency of the hardware trigger to identify $pp\gamma$ events. The procedure to obtain this efficiency is fully described in Ref. [40] and will not be repeated here.

TABLE VI. Overview of all the parameters used to convert the number of counts to an absolute cross section. Also see Eq. (2).

Description	Param.	Component	Method
Bin size	$\delta\mathcal{F}$	Standard	$\Delta\cos\theta_1\Delta\cos\theta_2$ $\Delta\phi_{event}\Delta\Phi\Delta\theta_\gamma/2$
Luminosity	$n_{inc}\rho\delta x$	Beam flux	Faraday cup
		Areal density	42.5 mg/cm^2
		Renormalization	Elastic *pp*
Detection efficiency	ϵ_{det}	MWPC	MWPC analysis
		TAPS cuts	Monte Carlo
		Trigger	LED-high analysis

E. Estimation of systematic errors

In order to convert the number of counts to a cross section, one has to apply Eq. (2). The parameters used in this equation are listed in Table VI. The determination of all these parameters is discussed in the previous sections of this chapter. In Fig. 15 the time dependence of the various efficiencies is shown. The sources of error in the measured observables can be separated into statistical and systematic. The determination of the statistical error is trivial, since one simply has to replace N_{det} by $\sqrt{N_{det}}$ in Eq. (2). The determination of the systematic error is more difficult, since no straightforward procedure exists. All the parameters listed in Table VI, in principle, introduce a systematic error.

In the determination of the luminosity, only the error in obtaining the elastic *pp* cross section is important, since the nominal luminosity cancels out. The error in the elastic cross section is given by statistics and the error associated with estimating the contribution of the background. The latter is not constant in time due to buildup of dirt on the ultra-cold target window foils. Since the background is rapidly decreasing at increasing polar scattering angle, only the elastic-scattering data from 15° to 23° are normalized to the predictions of SAID as was discussed in Sec. III B. The background contribution is determined to be 3% with the empty-target run. This 3% is corrected for in the normalization. The systematic error in this procedure is generously estimated to be 1%. The statistical error in the elastic data of all the runs is negligible.

The error in the determination of the wire-chamber efficiency is given by statistics. This statistical error was always less than 1%. Instead of propagating this error on a bin-to-bin basis, a systematic error of 1% is used for the wire-chamber efficiency determination.

The error due to the corrections made with the Monte Carlo code GEANT is difficult to estimate. The quality of GEANT simulations for TAPS is investigated in Ref. [38]. The agreement between the simulated energy response and the measured energy response is found to be very good. Therefore, the error made in the correction factor coming from the response of the photon detector due to the $E_\gamma > 20$ MeV cut is neglected. The error which is considered to dominate this correction is the accuracy to which the geometry of the experiment is described in GEANT. In the case of a full coverage

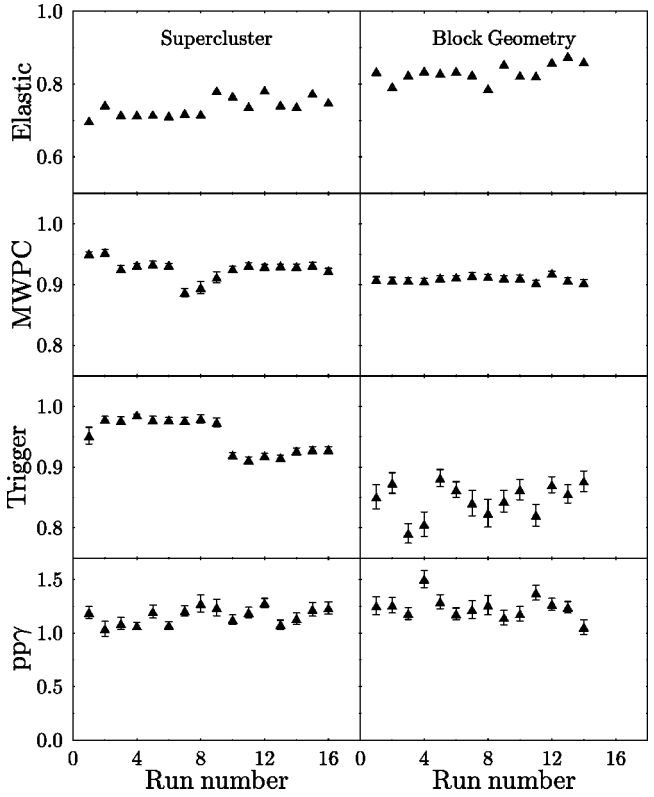

FIG. 15. The time dependence of the various components which enter in the calculation of the $pp\gamma$ cross section. The data have been split into sets which were taken subsequently in time. Going from top to bottom, the plots show the renormalization of the luminosity as found with the elastic proton-proton channel, the wire-chamber efficiency at $\theta = 16°$, the trigger efficiency and the normalized $pp\gamma$ cross section for a specific bin. The time spans a period of a few weeks of running.

of the solid angle, the corrections made with GEANT are small. In the case of an incomplete solid-angle coverage, the geometrical factor can exceed 5, but the accuracy of this factor resides in simulating the edges of the detectors. Even if the simulation of these edge-effects is not more accurate than 30%, the total correction factor is still quite accurate. For TAPS positioned in the block geometry, the systematic error is estimated to be 5%. For TAPS in the supercluster geometry, the positions of the crystals in GEANT and the nominal positions in the experiment matched exactly. Furthermore, a geometrical correction factor is absent since the azimuthal coverage in this experiment is complete for a large part of the detector. Therefore, the Monte Carlo simulations in this experiment are estimated to be accurate to a 3% level.

The error in the trigger efficiency is governed by the statistical error. For all the runs it is at most 2%. Therefore, the systematic error due to the trigger efficiency is estimated to be 2%. The last source of systematic errors resides in the subtraction of the background. The contribution of the background itself is at most 5% (see Fig. 13). The systematic error introduced by this procedure is estimated to be 1%.

All the errors and their contributions to the total systematic error are listed in Table VII. In principle, one has to

TABLE VII. Sources of systematic errors.

Source	Supercl.	Block
Elastic *pp*	1%	1%
Trigger efficiency	2%	2%
Monte Carlo simulation	3%	5%
Wire-chamber efficiency	1%	1%
Background	1%	1%

divide the systematic error in two classes, namely the class of errors acting on the overall normalization of the cross section only, and the class of errors affecting the relative values of the cross section in different bins. This division is, however, dependent on the form of presentation of the data. The effect of Monte Carlo simulations, for example, affects the relative position of points with different θ_γ. However, for data points with the same θ_γ, this error can be classified as an error affecting the overall normalization only. The error in the elastic cross section is always an overall error. In the presentation of the data in the following section, care has been taken to keep track of these errors as accurately as possible.

F. Determination of the analyzing powers

Under the assumption of parity conservation, one can show that for *coplanar* scattering (all momenta in one plane) the cross section is a function of $\mathbf{P}\cdot\hat{\mathbf{n}}$, where $\mathbf{P}$ is the polarization vector and $\hat{\mathbf{n}}$ is the unit vector normal to the scattering plane. The most general form of the cross section is expressed in Eq. (3), which only depends on one analyzing power. However, in the case of noncoplanar scattering, one can construct three independent axial vectors, resulting in three analyzing powers. These three analyzing powers constitute an axial vector $\mathbf{A}$. The cross section is then given by the following expression:

$$\frac{d\sigma^{pol}}{d\Omega_1 d\Omega_2 d\theta_\gamma} = \frac{d\sigma^0}{d\Omega_1 d\Omega_2 d\theta_\gamma}(1+\mathbf{P}\cdot\mathbf{A}) = \frac{d\sigma^0}{d\Omega_1 d\Omega_2 d\theta_\gamma}(1+pA_\gamma^\perp\cos\phi_\gamma + pA_\gamma\sin\phi_\gamma). \quad (6)$$

Here, we introduce $A_\gamma^\perp$ and A_γ to denominate the analyzing powers, since the names A_y and A_x are more commonly associated with a different definition of the scattering plane [45]. In this convention, ϕ_γ is defined with respect to the plane perpendicular to the polarization vector. In Eq. (6) the dependence on A_z drops out, since it can only be measured with a polarization component in the direction of the beam, which was not present in our experiment. The observables $A_\gamma^\perp$ and A_γ are linear combinations of A_x and A_y. In coplanar kinematics $A_\gamma^\perp$ reduces to A_y.

In order to extract analyzing powers, the collected data are grouped according to the polarization state of the beam. The measured analyzing power $A_\gamma^\perp$ is then given by

$$A_\gamma^\perp = \frac{1}{G_\gamma^\perp p_y}\frac{N_L^\uparrow/N_L^0 - N_R^\uparrow/N_R^0}{N_L^\uparrow/N_L^0 + N_R^\uparrow/N_R^0}, \quad (7)$$

where N_L is the number of events with $\phi_\gamma<90°$ or $\phi_\gamma>270°$ and N_R is the number of events with $90°<\phi_\gamma<270°$. The markers $\uparrow$ and 0 indicate a polarized-beam state and unpolarized-beam state, respectively. The beam polarization p_y is determined from the elastic proton-proton scattering. The variable $G_\gamma^\perp$ is a geometrical factor accounting for detector acceptance, which is determined with a Monte Carlo simulation. The analyzing powers as determined with the two different states of beam polarization are, after consistency checks, combined to one set in order to increase the statistical accuracy.

The analyzing power A_γ is extracted in the same fashion with the only difference being that one has to measure the top-bottom asymmetry:

$$A_\gamma = \frac{1}{G_\gamma\ p_y}\frac{N_T^\uparrow/N_T^0 - N_B^\uparrow/N_B^0}{N_T^\uparrow/N_T^0 + N_B^\uparrow/N_B^0}, \quad (8)$$

where N_T is the number of counts with $\phi_\gamma<180°$ and N_B is the number of counts with $\phi_\gamma>180°$. The geometrical factor, G_γ, is again determined with Monte Carlo simulations.

IV. DISCUSSION OF EXPERIMENTAL RESULTS ALONG WITH THEORETICAL CALCULATIONS

In this section the experimental results are presented. The total amount of $pp\gamma$ data in the experiment in which TAPS was configured in the supercluster geometry comprises 4 million events. The other experiment, in which TAPS was configured in the block geometry, comprises a total of 6 million events. The total number of data points (bins) one obtains from these sets is estimated as follows. One has to bin the data in 4 variables, namely two proton polar angles, θ_1, θ_2, the photon polar angle θ_γ, and the noncoplanarity angle Φ as defined later in Eq. (A12) and Fig. 23. The data are not binned in the fifth parameter, ϕ_{event} (see Fig. 23), since the cross section is invariant under a rotation around the beam axis when the beam is not polarized. With the beam polarized, the variations in this angle yield a value for the analyzing power. The bin-size in each of the proton angles (θ_1 and θ_2) is 2°, resulting in a total of 9 bins. The bin-size in θ_γ is 10°, resulting in 3 bins in the supercluster experiment (135°, 145° and 155°) and 8 bins in the block-geometry experiment (65°, 75°, 85°, 105°, 115°, 125°, 145° and 155°). The number of bins in the noncoplanarity angle is less readily derived, since the maximally allowed noncoplanarity angle is dependent on the other three kinematic parameters. A simulation reveals that, *on average*, the maximal noncoplanarity angle lies at 14° for the supercluster-geometry experiment and 26° for the block-geometry experiment. With a bin-size of 5°, this yields an average of 2 and 5 bins, respectively. Multiplying these numbers yields a total of approximately 650 bins for the supercluster-geometry experiment and 3650 bins for the block-geometry experiment. However, for both protons to be detected in SALAD, they need to have an energy above the threshold of 20 MeV. In order to obtain the

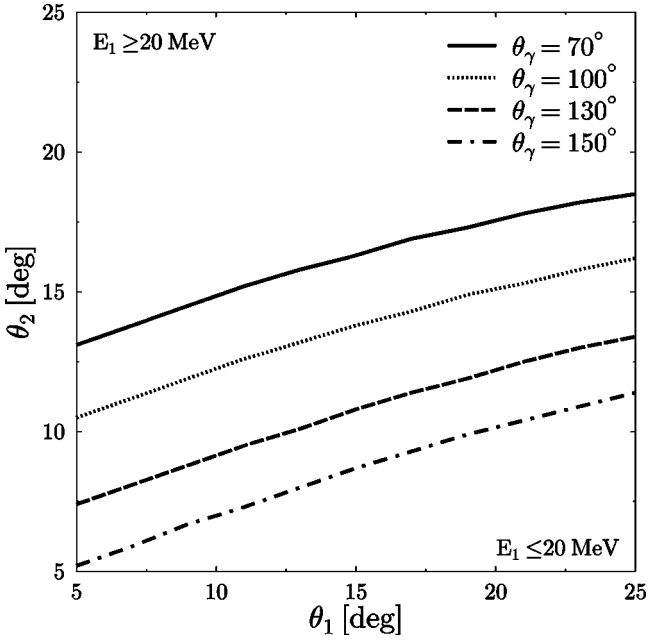

FIG. 16. Combinations of θ_1 and θ_2, which can be detected in the setup. The four lines indicate where $E_1=20$ MeV for $\theta_\gamma=70°$ (solid line), $\theta_\gamma=100°$ (dotted line), $\theta_\gamma=130°$ (dashed line), and $\theta_\gamma=150°$ (dash-dotted line). In the region above a line, both proton energies are larger than the detection threshold, while E_1 is lower in the region below it.

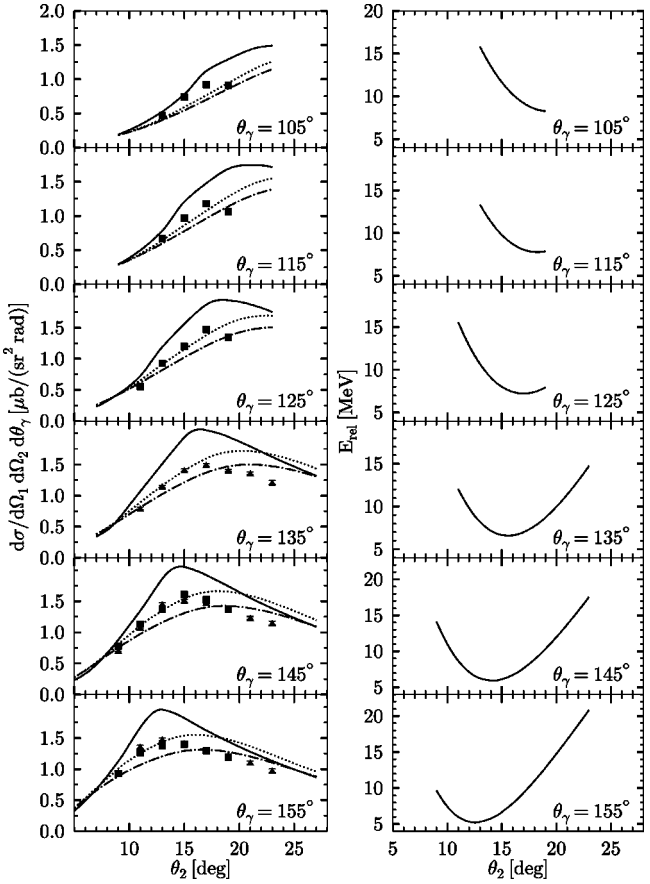

FIG. 17. Cross sections for coplanar geometry at $\theta_1=9°$ as a function of θ_2 for various photon polar angles. Data points shown with triangles and squares are from the supercluster- and block-geometry experiments, respectively. The angle-to-angle systematic error of 2% has been added linearly to the negligible statistical errors of the cross sections. The overall error in the supercluster and block geometries are 4% and 6%, respectively, and have not been included in the figure. The calculations are the fully microscopic (solid line), *tu*-SPM (dotted line) and *sk*-SPM (dash-dotted line). The corresponding relative energy versus θ_2 is shown in the right panel.

effective number of bins which are available from the two data sets, the $pp\gamma$ kinematics has been solved on a grid, spanning the complete phase space covered by the experimental setups. The total number of bins that are effectively available from the experiment is 434 for the supercluster geometry and 1480 for the block geometry. Some of the data obtained, namely the ones where the photon has scattered to very forward angles, suffer from higher experimental background and need more attention. The θ_γ bins of 65° and 75° will, therefore, not be presented to preserve the high accuracy of the measurements. A very large number of bins that remain still cannot be presented completely in this paper, since this would require over 200 plots. Therefore, a representative sample of the data not published before in Refs. [31–33] will be shown. A note should be added here about the data published in Refs. [32,33]. The analyzing powers presented in these papers which were obtained from the block-geometry experiment have a mistake in their sign and should be multiplied by −1.

Instead of showing the data as a function of all four variables as was done in the past references, the data will be shown for a sample of kinematics as a function of some of these variables and then as a function of a new variable, E_{rel}, defined in the Introduction. It should be pointed out that the combination of proton scattering angles cannot be chosen at random, because one of the protons might have an energy below the detection threshold of SALAD. This is illustrated in Fig. 16. The four lines indicate the coplanar combinations of θ_1, θ_2 and θ_γ, where $E_1=20$ MeV. Note that E_2 always happens to be larger than 20 MeV at these kinematics. Every combination of θ_1 and θ_2 above the lines has both proton energies above the 20 MeV detection threshold in SALAD. All combinations below the lines have $E_1<20$ MeV, and are thus not "detected" by SALAD.

A. Block- and supercluster-geometry data at selected kinematics

In this subsection the data taken with the supercluster and block geometries for coplanar kinematics are compared. This is done in Figs. 17 and 19 for the cross sections and Figs. 18 and 20 for the analyzing powers. They are also presented in Tables VIII and IX in Appendix B. The data are shown as a function of one of the outgoing proton angles, namely θ_2 for a fixed θ_1 (9° and 19°) and for various photon polar angles indicated in each panel in the figure. For $\theta_\gamma=135°$, $\theta_\gamma=145°$, and $\theta_\gamma=155°$ the data are shown for both geometries.

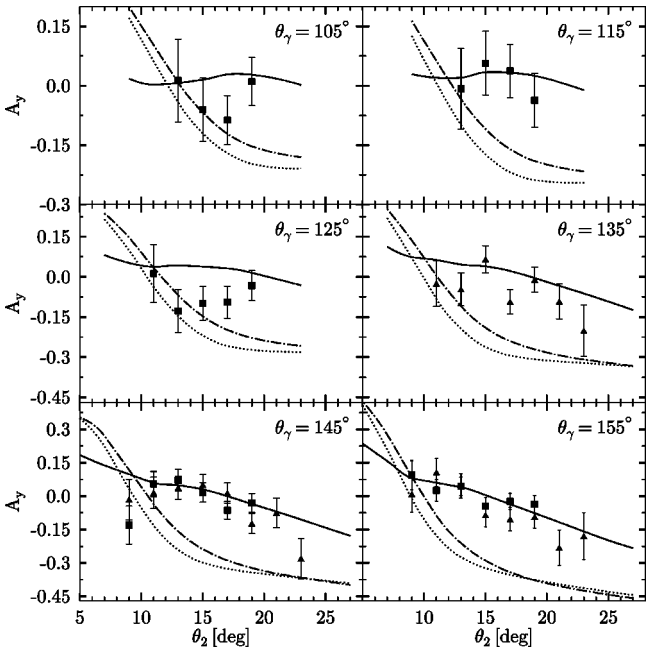

FIG. 18. The analyzing powers of the angle combinations shown in Fig. 17. The errors in the analyzing powers are dominated by statistics and the systematic errors of 2% are ignored. The explanation of the curves is the same as in Fig. 17.

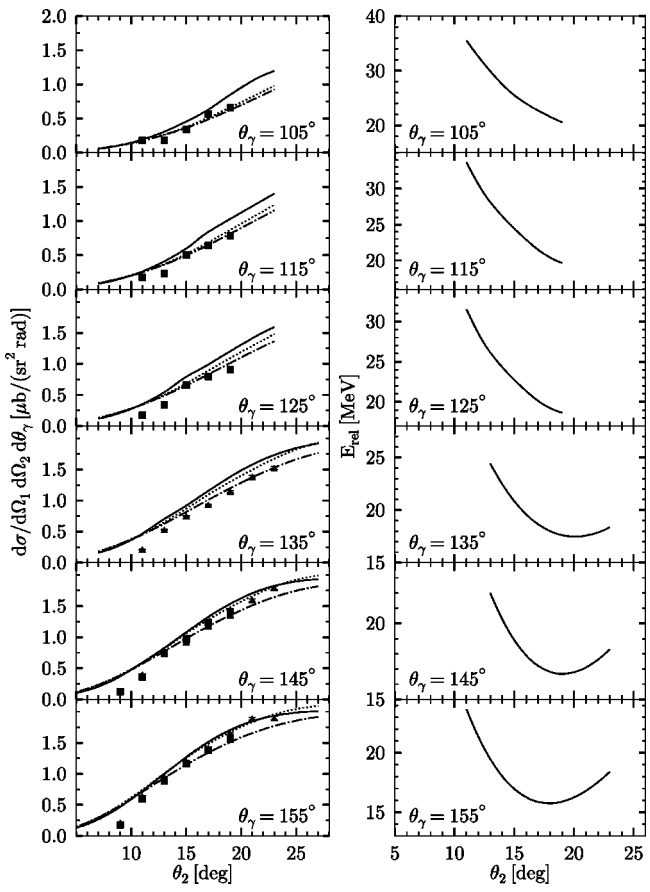

FIG. 19. The same as Fig. 17 except that $\theta_1 = 19°$.

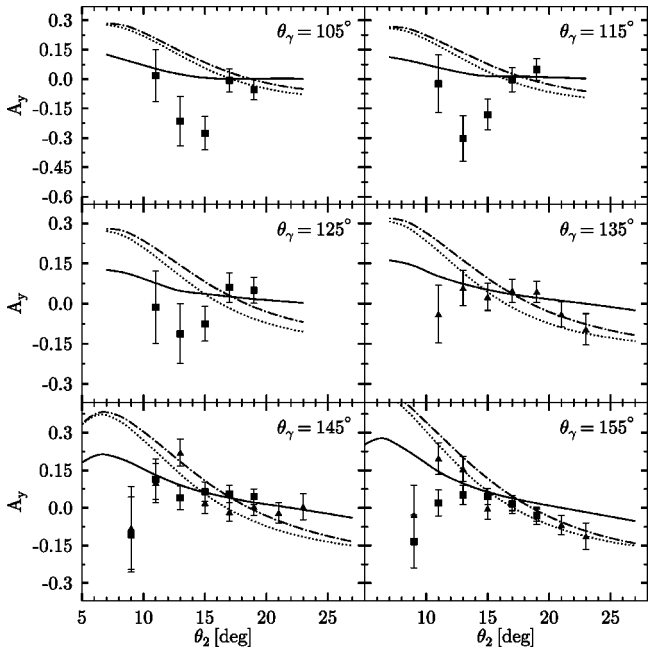

FIG. 20. The same as Fig. 18 except that $\theta_1 = 19°$.

For the block geometry, no data are available for proton angles 21° and 23°. At these angles, the azimuthal coverage for protons is no longer complete; therefore, photons will not be detected by TAPS for coplanar events. Taking a total systematic uncertainty of 4% and 6% for the supercluster and block geometries, respectively, into account (see Table VII), the experimental agreement between the two measurements is very good where there is an overlap between the two measurements. For the analyzing powers, the statistical errors are dominant. The good agreement for the cross sections and analyzing powers for the two geometries is observed for all the kinematics investigated and lends confidence in our estimation of the errors.

The data are compared to two different Soft Photon Models (SPM), dotted and dashed-dotted lines, in Figs. 17–20. In a SPM the amplitude for the bremsstrahlung process is formulated in a semi-microscopic way such that the soft-photon theorem is obeyed. The first of these SPMs is based on the model originally proposed in [7], later refined in [8,9], and will be referred to as *tu*-SPM. In the *tu*-SPM the *pp* T-matrix is evaluated at an on-shell point defined by the *t* and *u* Mandelstam variables calculated from the three on-shell legs for each of the four Born diagrams contributing to bremsstrahlung. To comply with the soft-photon theorem, this leading contribution is supplemented by a term to restore gauge invariance and isospin symmetry. The second SPM, "*sk*-SPM" is formulated in line with the original soft-photon theorem, and is similar to the so-called "low-SPM" [9] in the sense that the SPM is formulated in terms of derivatives of the *pp* T-matrix. In the "*sk*-SPM," however, also terms are kept which contain both a derivative of the *pp* T-matrix and the proton anomalous magnetic moment. All other terms are the same. While the "low-SPM" predictions fall considerably below the data for cross sections, the "*sk*-SPM" shows a rather good agreement.

The results of the microscopic calculations including ingredients depicted in Fig. 1 [14,18,48] are shown as solid curves in the figures. There is a large difference in the predictions of the different models. For the kinematics presented here (and even moreso for those presented in Refs. [31–33]), the *tu*-SPM reproduces the cross sections best among the SPMs. The microscopic model, however, seem to reproduce the shapes of the cross sections better than the SPMs. This was established by performing a fit of the data shown in Fig. 17. In this fit, a normalization factor was varied separately for each θ_γ to minimize the resulting χ^2. The reduced χ^2 obtained from these fits were around 5 (40) for the microscopic model (*tu*-SPM). The calculations of Eden and Gari [13] (not shown in the figure) also have the same shape in the angular distributions as the microscopic model but with much larger absolute magnitudes. The difference between these two calculations is not understood. For the analyzing powers, the microscopic calculations do a better job than the SPMs and come very close to almost all the data shown in the figures. This trend is also observed for the other kinematics not presented in this paper.

Another observation from Fig. 17 is that with increasing photon angle, a peak develops in the data which moves from large θ_2 to small θ_2. This peak is nicely reproduced by the microscopic calculations at large θ_γ and less so by the SPMs. Further inspection reveals that the peak position corresponds to a minimum of the quantity defined as relative energy, E_{rel}, in the introduction. The variations in this kinematic variable for the kinematics shown are presented in the right panel of Fig. 17. Here, one can clearly see how the nucleon-nucleon interaction is probed at different relative energies by simply varying the detection angles of photon and protons. This is one of the features that makes the bremsstrahlung process unique. From Eq. (1) in the Introduction, one can see that the sum of the variables E_{rel} and $E_\gamma^{\mathrm{c.m.}}$ is roughly constant for the beam energy of the present experiment. This means that the minimum of E_{rel} corresponds to the maximum of $E_\gamma^{\mathrm{c.m.}}$. The largest differences between the data and the microscopic calculations manifest themselves when E_{rel} is smallest or equivalently $E_\gamma^{\mathrm{c.m.}}$ is largest, i.e., when the nucleons during the interaction are farthest from their mass shell. The presence of the peak is the result of strong final-state interaction at small values of $E_{rel}(E_{rel}<10$ MeV). This feature is less pronounced in Fig. 19 since E_{rel} is generally larger ($E_{rel}>15$ MeV) for the kinematics shown in this figure, resulting in smaller final-state interactions.

In short, the high-precision data taken in the two different measurements agree well with each other and the systematic errors are well understood. The microscopic calculations reproduce the shape of the cross sections reasonably well, however, for certain kinematics where the relative energy between the two outgoing protons is small, there is a significant over prediction of the data by about 20%–30%. The source of this discrepancy is not understood. Since at the kinematics where the discrepancy is largest the relative energy in the emerging *pp* system is smallest, one would speculate that approximations in including the Coulomb force might be the problem. However a detailed investigation [48] has shown that this is not the case. In addition, the *pp* T-matrix used in the calculations has been improved in [48] over the earlier version used in the calculations [18]. The microscopic calculations also explicitly include non-nucleonic effects such as the Δ-resonance and magnetic meson-exchange contributions. Since these are generally small by themselves, it is unlikely that remaining uncertainties in the non-nucleonic effects would be the origin of the problem. A phenomenological study of different off-shell extrapolations of the magnetic $NN\gamma$ vertex [19] shows that these indeed may affect the cross section for kinematics where the large difference with the data is observed. Due to the fact that off-shell extrapolations are representation dependent, the observed effect in [19] could as well mimic dynamics in the *NN* interaction or a contact term. The physics for such an effect is an open issue but could for example reflect the importance of certain pion loop corrections which are related to the proximity of the pion production threshold.

Although the microscopic calculation shown in Figs. 18 and 20 come close to almost all the analyzing-power data and seem to perform much better than the SPMs, no strong conclusions can be drawn owing to the limited statistical accuracy of the data. In general, one should use the SPMs with some care when comparing to the data, since various prescriptions, which all satisfy the soft-photon theorem, may result in very different results for cross sections and analyzing powers.

B. Alternative presentation of the cross-section data

As was mentioned at the beginning of this section, it is practically impossible to present all data points measured in the present experiment. Instead, it is chosen to study the differences between the measured and the calculated cross sections as a function of some selected kinematical variables. This is done with the hope of understanding the differences that have persisted between the results of the microscopic calculations and the experimental results. In presenting the data in this manner though, one loses the dependence on all other kinematical variables. More than 1000 bins at various scattering angles for coplanar and noncoplanar geometries, where the acceptance was 100%, have been taken to make the "difference" plot.

The variable used here was already defined in the Introduction as the relative energy, E_{rel}. One can now take all data points (from both geometries) and calculate the difference between the cross-section results from the microscopic calculations and the experimental measurements. These differences are shown in Fig. 21 as a function of E_{rel} or equivalently $E_\gamma^{\mathrm{c.m.}}$ in a contour plot. Various contours (z-axis) represent the density of data points giving the same difference for the same E_{rel}. The smooth curve represents the average density of points.

As can be seen, the discrepancies between the results from the theoretical calculation and the experiments become larger as the relative energy, E_{rel}, becomes smaller. The same figure was made in Ref. 33 for kinematics presented there. The deviations shown there were so large that a revision [48] of the Fleischer-Tjon potential [46] was made. Even with the most recent version, used in the present work, there seems to be still some problems remaining. To understand this picture

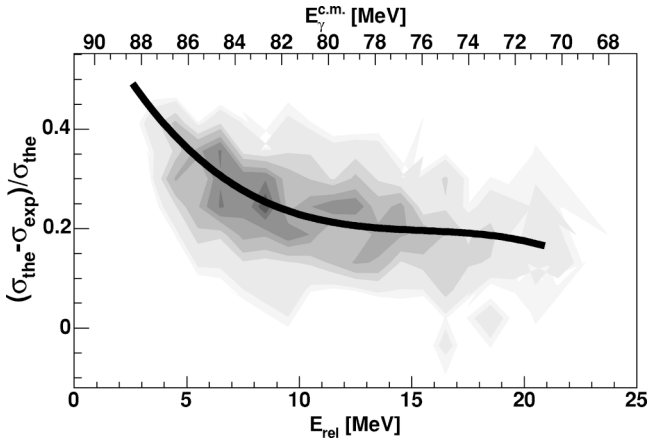

FIG. 21. The relative difference between the experimental and theoretical cross sections as a function of E_{rel} and $E_\gamma^{\text{c.m.}}$. The calculations used to obtain the differences are the microscopic calculations of Martinus *et al.* (Ref. [18]).

better, the kinematical variable $E_\gamma^{\text{c.m.}}$ is shown on top of the panel. The reason for plotting the data as such is to make clear that the differences seen in Fig. 21 may be due to the low-energy behavior of the potential as one discusses the relative energy of the outgoing particles, but may also be due to ingredients of the calculation which depend on the photon momentum. It is clear from Fig. 21 that the discrepancy increases as a function of the photon energy. One possibility might be that the magnetic terms are estimated to be too large. Note also that the difference is becoming smaller as the photon energy decreases. This should be a reflection of the fact that the predictions of the calculations all converge at the elastic limit. The more recent measurements at KVI [49], to study lower photon energies, aim at this aspect of the investigation.

The differences between the theory and the data were plotted as a function of several kinematic variables, but no correlation between the differences and the variables were seen. These sorts of figures should serve as a guide in the search for possible sources of problems which cause the theory to deviate from the data at the level of 20% to 30%. It was shown in the last subsection how these differences behave as a function of angle. The relevant parameter seems to be E_{rel} as can be deduced from Fig. 21.

V. SUMMARY AND CONCLUSIONS

At KVI, Groningen, a series of measurements has been performed at 190 MeV beam energy with the aim to measure proton-proton bremsstrahlung cross sections and analyzing powers with high precision. For the detection of the outgoing protons, SALAD was used. This detector was specifically designed and built for these experiments [37]. It has a large solid angle of 400 msr and allows one to make cylindrically-symmetric measurements around the beam axis for most of the polar angular range. The covered polar angles range from 6° to 26°. The detector consists of two wire chambers [39] with a central hole for beam passage followed by two segmented stacks of scintillators. The system is capable of handling high count rates and allows a hardware trigger rejection of protons stemming from elastic scattering [40].

For the detection of the bremsstrahlung photons, we have used TAPS [38]. In this campaign, TAPS consisted of approximately 400 BaF_2 crystals, which were used in two different geometries. In the first geometry, all crystals were mounted at backward angles in a large hexagon, surrounding the beam pipe. This results in a polar angular range of $125° - 170°$ and a complete azimuthal coverage. This cylindrical symmetry is essential for obtaining high statistics in cross sections and analyzing powers and specifically to measure a second analyzing power (A_x) which requires the measurement of the photons in a large range of the azimuthal angle. In order to investigate the angular distribution of the photons, a second experiment was performed where the cylindrical symmetry in photon detection was sacrificed. This second geometry, consists of six rectangular frames, each containing 64 crystals. These frames were positioned around the target on both sides of the beam pipe.

Only 2% of the collected events are bremsstrahlung events, the rest being the background that could not be eliminated by the trigger. In order to obtain a clean bremsstrahlung signal from the data, a cut is set on the time-of-flight in TAPS to discriminate massive particles from photons. In addition the over-determined kinematics of the reaction is used to reduce the background to a negligible level.

For an accurate determination of the observables, one needs to determine the luminosity and the degree of beam polarization. This is done by comparing the measured angular distribution of *pp* elastic scattering with two phase-shift analyses, from VPI [44] and Nijmegen [1]. A fit was made with only the luminosity and the beam polarization as free parameters. The agreement with both phase-shift analyses is excellent. The typical value for the degree of beam polarization is 0.65, with an accuracy of 0.01. The total detection efficiency of the system exceeds 80% and the geometrical acceptance of the system, estimated with GEANT, ranges, in all cases, from 20% to 100%. The systematic error on the cross-section data with the TAPS detector in the supercluster geometry is 4%. The error on the cross sections produced with TAPS in the block geometry is 6%. The error in the analyzing powers is dominated by statistics.

The two $pp\gamma$ experiments have overlapping coverage. Both the cross sections and analyzing powers of the two experiments are in excellent agreement with each other. Also an earlier cross section measurement [47], performed at a slightly higher energy (200 MeV), and with much less accuracy is in agreement with cross sections measured in the present experiment.

The experimental data are compared with the results of calculations based on Soft-Photon Models and the relativistic microscopic calculation of Martinus *et al.* [14,18,48]. The latter model includes, in addition to a consistent propagation of the intermediate off-shell nucleons, higher-order contributions like the magnetic meson-exchange currents, the Δ-isobar and negative-energy states. The overall agreement of the experimental cross sections with the microscopic calculation is fair as far as the shape of the angular distributions is concerned. However, this calculation seems to overesti-

mate the cross sections almost everywhere in phase space. The results of the microscopic calculations are satisfactory when compared to the experimental analyzing powers, albeit with limited statistical accuracy. The SPM calculations come closer to the experimental cross sections in magnitude even though the shapes are not as well reproduced as they are by the microscopic calculation. There are sizable differences between various SPMs. However, they all fail to describe the data for the analyzing powers.

A close inspection of the bulk of the cross-section data shows that differences from the results of the calculations are largest where the relative energy, E_{rel}, of the two outgoing protons is smallest, or equivalently, the photon energy in the center of mass, $E_\gamma^{\text{c.m.}}$ is highest. The origin of these 20%–30% discrepancies as discussed in Sec. IV B is not yet understood. It might reside either in the sector dealing with *NN* interaction or in the ingredients dealing with the coupling of the photons to a proton. To distinguish between these two effects, one needs to study the reaction as a function of E_{rel} and $E_\gamma^{\text{c.m.}}$ separately. For any beam energy, these two are correlated to each other, and measuring one is equivalent to measuring the other. To study, in more detail, the differences at smaller photon energies in the center of mass, a recent experiment has been performed at KVI with the same beam energy. This experiment aims at investigating the cross sections at kinematics approaching the elastic limit. Here, the microscopic calculations and those based on the soft-photon theorem begin to converge and should agree better with the data. The data of that experiment are being analyzed presently. Finally, it is desirable to perform an experiment at different beam energies to change the scale between E_{rel} and $E_\gamma^{\text{c.m.}}$. The result of such an experiment coupled to those presented here and those of the experiment performed recently at KVI should shed some light on the issue of whether discrepancies between the data and the calculations, as observed in the present measurement, have their roots in the hadronic sector or the photon coupling.

ACKNOWLEDGMENTS

The authors acknowledge the support by the TAPS collaboration in bringing TAPS into operation at KVI. They also express their appreciation for the tireless efforts of the cyclotron and ion-source groups in delivering the high-quality beam used in these measurements. The help of R. Timmermans and M. C. M. Rentmeester in providing the normalization of the elastic *pp* data is appreciated. R. Timmermans should also be thanked for providing valuable comments on the manuscript. This work is part of the research program of the "Stichting voor Fundamenteel Onderzoek der Materie" (FOM) with financial support from the "Nederlandse Organisatie voor Wetenschappelijk Onderzoek" (NWO).

APPENDIX A: KINEMATICS

In this appendix the kinematics of the $pp\gamma$ reaction is discussed. The procedure used in the data analysis for solving the kinematic equations in spherical coordinates is outlined. The definitions used here are similar to the ones used by Drechsel and Maximon [45], but differ in details. These differences are introduced, because this experiment is performed with a polarized beam, which complicates the picture to some extent when determining the analyzing power.

1. Solving the kinematic equations

A $pp\gamma$ event is described by the momentum vectors of the three outgoing particles. Each momentum vector has three components, and the final state has thus nine parameters, which describe it completely. These nine parameters are, however, not independent, because of the laws of energy and momentum conservation. These four conservation laws reduce the number of independent parameters to five. In the laboratory system, the *z*-axis is chosen along the direction of the incoming proton, which has momentum $\mathbf{p_b}$. The *y*-axis is chosen along the direction of polarization of the beam, orthogonal to $\hat{z}$. The *x*-axis completes the right-handed set of orthogonal directions. The target proton has zero momentum. The momenta of the two outgoing protons are $\mathbf{p_A}$ and $\mathbf{p_B}$. The momentum of the photon is $\mathbf{k}$. The energy and momentum conservation laws now yield (natural units, $\hbar = c = 1$ are used)

$$\mathbf{p_A} + \mathbf{p_B} + \mathbf{k} = \mathbf{p_b}, \tag{A1}$$

$$\sqrt{p_A^2 + m_p^2} + \sqrt{p_B^2 + m_p^2} + k = \sqrt{p_b^2 + m_p^2} + m_p. \tag{A2}$$

Here, m_p is the mass of the proton. The conventional choice of the five parameters to fix the kinematics are the spherical angles of the momenta: θ_A, ϕ_A, θ_B, ϕ_B and θ_γ. The conservation laws for momentum in spherical coordinates are

$$p_A \sin\theta_A \cos\phi_A + p_B \sin\theta_B \cos\phi_B + k \sin\theta_\gamma \cos\phi_\gamma = 0, \tag{A3}$$

$$p_A \sin\theta_A \sin\phi_A + p_B \sin\theta_B \sin\phi_B + k \sin\theta_\gamma \sin\phi_\gamma = 0, \tag{A4}$$

$$p_A \cos\theta_A + p_B \cos\theta_B + k \cos\theta_\gamma = p_b. \tag{A5}$$

From the law of energy conservation (A2) the photon momentum can be expressed as

$$k = \sqrt{p_b^2 + m_p^2} + m_p - \sqrt{p_A^2 + m_p^2} - \sqrt{p_B^2 + m_p^2}. \tag{A6}$$

If one substitutes this expression for k in Eq. (A5), it can be solved for p_B:

$$p_B = \frac{q \cos\theta_B \pm \sqrt{q^2 \cos^2\theta_\gamma - m_p^2 \cos^2\theta_\gamma (\cos^2\theta_\gamma - \cos^2\theta_B)}}{\cos^2\theta_\gamma - \cos^2\theta_B} \tag{A7}$$

where q is defined as

$$q = p_A \cos\theta_A + (\sqrt{p_b^2 + m_p^2} + m_p - \sqrt{p_A^2 + m_p^2}) \cos\theta_\gamma - p_b. \tag{A8}$$

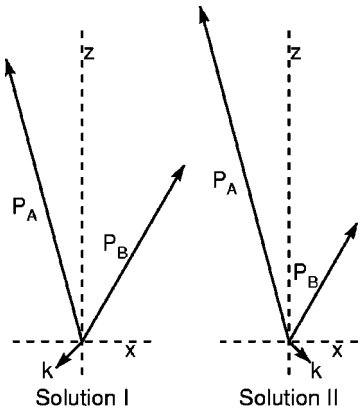

FIG. 22. The two different solutions of the kinematic equations with the same θ_A, θ_B, θ_γ, ϕ_A and ϕ_B.

With some algebra, one can eliminate ϕ_γ from Eqs. (A3) and (A4):

$$k^2\sin^2\theta_\gamma = (p_A \sin\theta_A - p_B \sin\theta_B)^2 + 4p_A p_B \sin\theta_A \sin\theta_B \sin^2\Phi', \quad \text{(A9)}$$

Here, the new variable Φ' is defined as

$$\Phi' = \frac{\pi}{2} + \frac{\phi_A - \phi_B}{2}. \quad \text{(A10)}$$

In Eq. (A9) one can substitute k from Eq. (A6) and p_B from Eq. (A7). The resulting expression has only p_A as an unknown, and can be solved by numerical means.

2. Conventions for the kinematics

From Eq. (A7) it can be seen that there are in general two possible choices for p_B given a certain p_A. Furthermore, it turns out that Eq. (A9) has in general two solutions, resulting in a total of four different mathematical solutions. Two of these solutions are nonphysical in the sense that they produce negative values for either p_A, p_B or k. The other two solutions are valid solutions of the kinematic equations, given θ_A, ϕ_A, θ_B, ϕ_B and θ_γ. The labels A and B have been assigned arbitrarily to the two protons. By assigning labels 1 and 2 to the two protons in a unique way, one can discriminate between the two different solutions. For the sake of the argument, the solution with the lowest value of p_A is called solution I and the other solution II, i.e., $p_A^I < p_A^{II}$. One can now adopt the convention to label p_A as p_1 and p_B as p_2 in case of solution I. In the case of solution II, it is the other way around: $A \Rightarrow 2$ and $B \Rightarrow 1$. This results in a unique labeling of the two protons, independent of the initial A, B labeling.

For the case of *coplanar* kinematics, the difference between the two solutions is depicted in Fig. 22. In the first possibility (solution I), the photon is emitted to the same side of the beam axis as proton A. For the other possibility (solution II), the photon is emitted to the same side as proton B. With the above definition, this means that proton 1 lies on the same side of the beam axis as the photon. Note that this interpretation holds only for coplanar scattering. In the case of noncoplanar scattering, the definition of protons 1 and 2 is still unique, but a trivial interpretation is not always available.

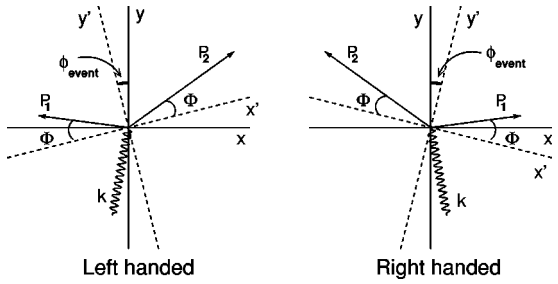

FIG. 23. The geometrical interpretation of Φ and ϕ_{event}. In a right-handed system Φ is defined as positive and as negative in a left-handed system.

With protons 1 and 2 so defined, the three vectors $\mathbf{p}_1$, $\mathbf{p}_2$, and $\mathbf{k}$ can either form a right-handed system, where $(\mathbf{p}_1 \times \mathbf{p}_2)\cdot\mathbf{k} > 0$ or a left-handed system, where $(\mathbf{p}_1 \times \mathbf{p}_2)\cdot\mathbf{k} < 0$. These two situations are depicted in Fig. 23. The "parity" Π of a $pp\gamma$ event is now defined as the sign of this vector product:

$$\Pi = \text{sign}[(\mathbf{p}_1 \times \mathbf{p}_2)\cdot\mathbf{k}]. \quad \text{(A11)}$$

From Eq. (A10) one can see that in the case of coplanar kinematics Φ' is either 0 or π. In this special case the parity Π is not defined, since the vector product in Eq. (A11) yields 0. One can define a second coordinate system for each event in such a manner that it is rotated around the beam direction with respect to the external coordinates. The x'-axis is chosen such that proton 1 makes an angle Φ with the positive x'-axis and proton 2 makes an angle Φ with its negative part. The y'-axis is orthogonal to the x'-z plane. Since the angle Φ in this new coordinate system is 0 for coplanar events, it is referred to as the "noncoplanarity angle." One can define it as

$$\Phi = \Pi \ \text{asin}(|\sin(\Phi')|) \quad \text{(A12)}$$

where Π is the parity of the event and Φ' is defined in Eq. (A10). Using this definition, the noncoplanarity angle contains the information on the handedness of the vectors $\mathbf{p_A}$, $\mathbf{p_B}$ and $\mathbf{k}$. The ambiguity of Π in the coplanar case is then solved in a natural way. The angle Φ lies between $-\pi/2$ and $\pi/2$. The external coordinate system and the coordinate system of the event make an angle which is called ϕ_{event}. The geometrical interpretation of the noncoplanarity angle and ϕ_{event} is depicted in Fig. 23.

APPENDIX B: DATA TABLES

TABLE VIII. Cross sections and analyzing powers for the supercluster-geometry data presented in Figs. 17 through 20. The cross sections are given in units of $\mu b/sr^2/rad$.

θ_1(deg)	θ_2(deg)	θ_γ(deg)	$d\sigma/d\Omega$	$\Delta d\sigma/d\Omega$	A_γ	ΔA_γ
9	11	135	0.796	0.018	−0.025	0.086
9	13	135	1.148	0.019	−0.047	0.061
9	15	135	1.409	0.020	0.066	0.051
9	17	135	1.493	0.019	−0.093	0.046
9	19	135	1.406	0.019	−0.010	0.046
9	21	135	1.359	0.024	−0.092	0.065
9	23	135	1.210	0.031	−0.201	0.095
9	9	145	0.704	0.018	−0.016	0.092
9	11	145	1.076	0.020	0.015	0.071
9	13	145	1.450	0.021	0.038	0.052
9	15	145	1.508	0.020	0.050	0.046
9	17	145	1.477	0.019	0.014	0.045
9	19	145	1.370	0.018	−0.123	0.046
9	21	145	1.232	0.023	−0.075	0.067
9	23	145	1.149	0.029	−0.281	0.091
9	9	155	0.950	0.022	0.009	0.079
9	11	155	1.360	0.023	0.106	0.063
9	13	155	1.476	0.022	0.047	0.055
9	15	155	1.417	0.021	−0.085	0.052
9	17	155	1.305	0.019	−0.104	0.052
9	19	155	1.222	0.018	−0.093	0.051
9	21	155	1.106	0.023	−0.232	0.080
9	23	155	0.973	0.029	−0.180	0.105
19	11	135	0.210	0.007	−0.039	0.108
19	13	135	0.530	0.010	0.059	0.065
19	15	135	0.749	0.011	0.025	0.051
19	17	135	0.929	0.011	0.048	0.044
19	19	135	1.145	0.012	0.045	0.039
19	21	135	1.381	0.018	−0.039	0.047
19	23	135	1.524	0.025	−0.096	0.059
19	9	145	0.119	0.005	−0.080	0.166
19	11	145	0.397	0.009	0.100	0.078
19	13	145	0.729	0.011	0.221	0.054
19	15	145	0.917	0.011	0.020	0.043
19	17	145	1.172	0.012	−0.016	0.037
19	19	145	1.346	0.013	0.004	0.033
19	21	145	1.599	0.019	−0.020	0.040
19	23	145	1.791	0.027	0.004	0.051
19	9	155	0.216	0.008	−0.027	0.119
19	11	155	0.637	0.012	0.198	0.063
19	13	155	0.944	0.013	0.156	0.050
19	15	155	1.196	0.014	−0.003	0.042
19	17	155	1.412	0.014	0.014	0.036
19	19	155	1.647	0.015	−0.032	0.034
19	21	155	1.890	0.021	−0.068	0.039
19	23	155	1.896	0.029	−0.113	0.053

TABLE IX. Same as Table VIII but for the block geometry.

θ_1(deg)	θ_2(deg)	θ_γ(deg)	$d\sigma/d\Omega$	$\Delta d\sigma/d\Omega$	A_γ	ΔA_γ
9	13	105	0.465	0.020	0.013	0.105
9	15	105	0.739	0.024	−0.060	0.080
9	17	105	0.920	0.025	−0.087	0.062
9	19	105	0.910	0.025	0.011	0.060
9	13	115	0.666	0.028	−0.007	0.102
9	15	115	0.968	0.031	0.057	0.081
9	17	115	1.177	0.032	0.038	0.067
9	19	115	1.061	0.030	−0.036	0.068
9	11	125	0.556	0.027	0.012	0.109
9	13	125	0.927	0.032	−0.127	0.081
9	15	125	1.201	0.033	−0.099	0.064
9	17	125	1.475	0.035	−0.094	0.060
9	19	125	1.343	0.033	−0.032	0.056
9	9	145	0.777	0.027	−0.130	0.086
9	11	145	1.131	0.030	0.054	0.057
9	13	145	1.377	0.030	0.071	0.049
9	15	145	1.609	0.031	0.016	0.044
9	17	145	1.528	0.028	−0.064	0.040
9	19	145	1.373	0.026	−0.031	0.043
9	9	155	0.927	0.026	0.094	0.065
9	11	155	1.267	0.028	0.025	0.049
9	13	155	1.373	0.027	0.044	0.042
9	15	155	1.400	0.025	−0.045	0.038
9	17	155	1.295	0.023	−0.024	0.037
9	19	155	1.193	0.022	−0.036	0.039
19	11	105	0.178	0.010	0.018	0.132
19	13	105	0.182	0.009	−0.215	0.125
19	15	105	0.335	0.012	−0.276	0.086
19	17	105	0.562	0.014	−0.006	0.059
19	19	105	0.660	0.015	−0.054	0.053
19	11	115	0.180	0.011	−0.024	0.147
19	13	115	0.229	0.012	−0.303	0.116
19	15	115	0.501	0.016	−0.181	0.079
19	17	115	0.644	0.017	−0.004	0.062
19	19	115	0.784	0.019	0.048	0.056
19	11	125	0.176	0.011	−0.013	0.136
19	13	125	0.342	0.014	−0.112	0.112
19	15	125	0.657	0.018	−0.075	0.064
19	17	125	0.797	0.019	0.061	0.055
19	19	125	0.909	0.020	0.050	0.049
19	9	145	0.121	0.008	−0.106	0.150
19	11	145	0.363	0.012	0.114	0.081
19	13	145	0.753	0.016	0.041	0.048
19	15	145	0.974	0.017	0.065	0.039
19	17	145	1.235	0.018	0.055	0.035
19	19	145	1.408	0.019	0.045	0.031
19	9	155	0.179	0.008	−0.133	0.106
19	11	155	0.595	0.014	0.020	0.052
19	13	155	0.889	0.016	0.052	0.038
19	15	155	1.164	0.016	0.046	0.031
19	17	155	1.387	0.017	0.016	0.027
19	19	155	1.553	0.018	−0.029	0.024

[1] V. G. J. Stoks *et al.*, Phys. Rev. C **48**, 792 (1993); **49**, 2950 (1994); M. C. M. Rentmeester *et al.*, Phys. Rev. Lett. **82**, 4992 (1999).
[2] R. Machleidt *et al.*, Phys. Rev. C **53**, R1483 (1996).
[3] R. B. Wiringa *et al.*, Phys. Rev. C **51**, 38 (1995).
[4] J. Ashkin and R. E. Marshak, Phys. Rev. **76**, 989 (1949).
[5] F. E. Low, Phys. Rev. **110**, 974 (1958).
[6] E. M. Nyman, Phys. Lett. B **25**, 135 (1967); Phys. Rev. **170**, 1628 (1968).
[7] M. K. Liou, D. Lin, and B. F. Gibson, Phys. Rev. C **47**, 973 (1993).
[8] M. K. Liou, R. Timmermans, and B. F. Gibson, Phys. Rev. C **54**, 1574 (1996); Phys. Lett. B **345**, 372 (1995).
[9] A. Yu. Korchin, O. Scholten, and D. Van Neck, Nucl. Phys. A **602**, 423 (1996); A. Yu. Korchin and O. Scholten, *ibid.* **581**, 493 (1995).
[10] M. I. Sobel and A. H. Cromer, Phys. Rev. **132**, 2698 (1963).
[11] V. Herrmann and K. Nakayama, Phys. Rev. C **45**, 1450 (1992).
[12] F. de Jong *et al.*, Phys. Lett. B **333**, 1 (1994).
[13] J. A. Eden and M. F. Gari, Phys. Rev. C **53**, 1102 (1996).
[14] G. H. Martinus, O. Scholten, and J. A. Tjon, Phys. Rev. C **58**, 686 (1998).
[15] F. de Jong, K. Nakayama, and T. S. H. Lee, Phys. Rev. C **51**, 2334 (1995).
[16] F. de Jong and K. Nakayama, Phys. Rev. C **52**, 2377 (1995).
[17] M. Jetter and H. W. Fearing, Phys. Rev. C **51**, 1666 (1995).
[18] G. H. Martinus, O. Scholten, and J. A. Tjon, Phys. Rev. C **56**, 2945 (1997); G. H. Martinus *et al.*, Few-Body Syst. **26**, 197 (1999).
[19] S. Kondratyuk, G. Martinus, and O. Scholten, Phys. Lett. B **418**, 20 (1998).
[20] Y. Li, M. K. Liou, and W. M. Schreiber, Phys. Rev. C **57**, 507 (1998).
[21] V. Herrmann *et al.*, Nucl. Phys. **A582**, 568 (1995); K. Nakayama (private communication).
[22] A. Katsogiannis *et al.*, Phys. Rev. C **49**, 2342 (1994).
[23] M. Jetter, H. Freitag, and H. V. von Geramb, Phys. Scr. **48**, 229 (1993); Nucl. Phys. **A553**, 665c (1993).
[24] B. Gottschalk, W. J. Shlaer, and K. H. Wang, Nucl. Phys. **A94**, 491 (1967).
[25] K. W. Rothe, P. F. M. Koehler, and E. H. Thorndike, Phys. Rev. **157**, 1247 (1967).
[26] K. Michaelian *et al.*, Phys. Rev. D **41**, 2689 (1990).
[27] B. v. Przewoski, H. O. Meyer, H. Nann, P. V. Pancella, S. F. Pate, R. E. Pollock, T. Rinckel, M. A. Ross, F. Sperisen, Phys. Rev. C **45**, 2001 (1992).
[28] R. Bilger *et al.*, Phys. Lett. B **429**, 195 (1998).
[29] J. Złomanczuk, A. Johansson, and the WASA-PROMICE collaboration, Nucl. Phys. **A631**, 622c (1998).
[30] K. Yasuda *et al.*, Phys. Rev. Lett. **82**, 4775 (1999).
[31] H. Huisman *et al.*, Phys. Rev. Lett. **83**, 4017 (1999).
[32] H. Huisman *et al.*, Phys. Lett. B **476**, 9 (2000).
[33] H. Huisman *et al.*, Phys. Rev. C **65**, 031001(R) (2002).
[34] L. Friedrich *et al.*, *Proceedings of the International Workshop on Polarized Beams and Polarized Targets*, edited by H. Paetz gen Schieck and L. Sydow (World Scientific, Singapore, 1996), p. 198.
[35] H. W. Schreuder, *Proceedings of the XVth International Conference on Cyclotrons and their Applications* (IOP Publishing, London, 1998), p. 592.
[36] N. Kalantar-Nayestanaki, J. Mulder, and J. Zijlstra, Nucl. Instrum. Methods Phys. Res. A **417**, 215 (1998).
[37] N. Kalantar-Nayestanaki *et al.*, Nucl. Instrum. Methods Phys. Res. A **444**, 591 (2000).
[38] A. R. Gabler *et al.*, Nucl. Instrum. Methods Phys. Res. A **346**, 168 (1994); H. Ströher, Nucl. Phys. News **6**, 7 (1996).
[39] M. Volkerts *et al.*, Nucl. Instrum. Methods Phys. Res. A **428**, 432 (1999).
[40] S. Schadmand *et al.*, Nucl. Instrum. Methods Phys. Res. A **423**, 174 (1999).
[41] W. R. Leo, *Techniques for Nuclear and Particle Physics Experiments* (Springer-Verlag, Berlin, 1994).
[42] CERN Program Library Long Writeup W **5013**.
[43] J. G. Messchendorp *et al.*, Phys. Rev. Lett. **82**, 2649 (1999); **83**, 2530 (1999); Phys. Rev. C **61**, 064007 (2000).
[44] R. A. Arndt *et al.*, Phys. Rev. C **56**, 3005 (1997).
[45] D. Drechsel and L. C. Maximon, Ann. Phys. (N.Y.) **49**, 403 (1968).
[46] J. Fleischer and J. A. Tjon, Nucl. Phys. **A84**, 375 (1974); Phys. Rev. D **15**, 2537 (1977); **21**, 87 (1980).
[47] J. G. Rogers *et al.*, Phys. Rev. C **22**, 2512 (1980).
[48] M. D. Cozma *et al.*, Phys. Rev. C **65**, 024001 (2002); **68**, 044 003 (2003).
[49] M. Mahjour-Shafiei, Ph.D thesis, University of Groningen, 2004.